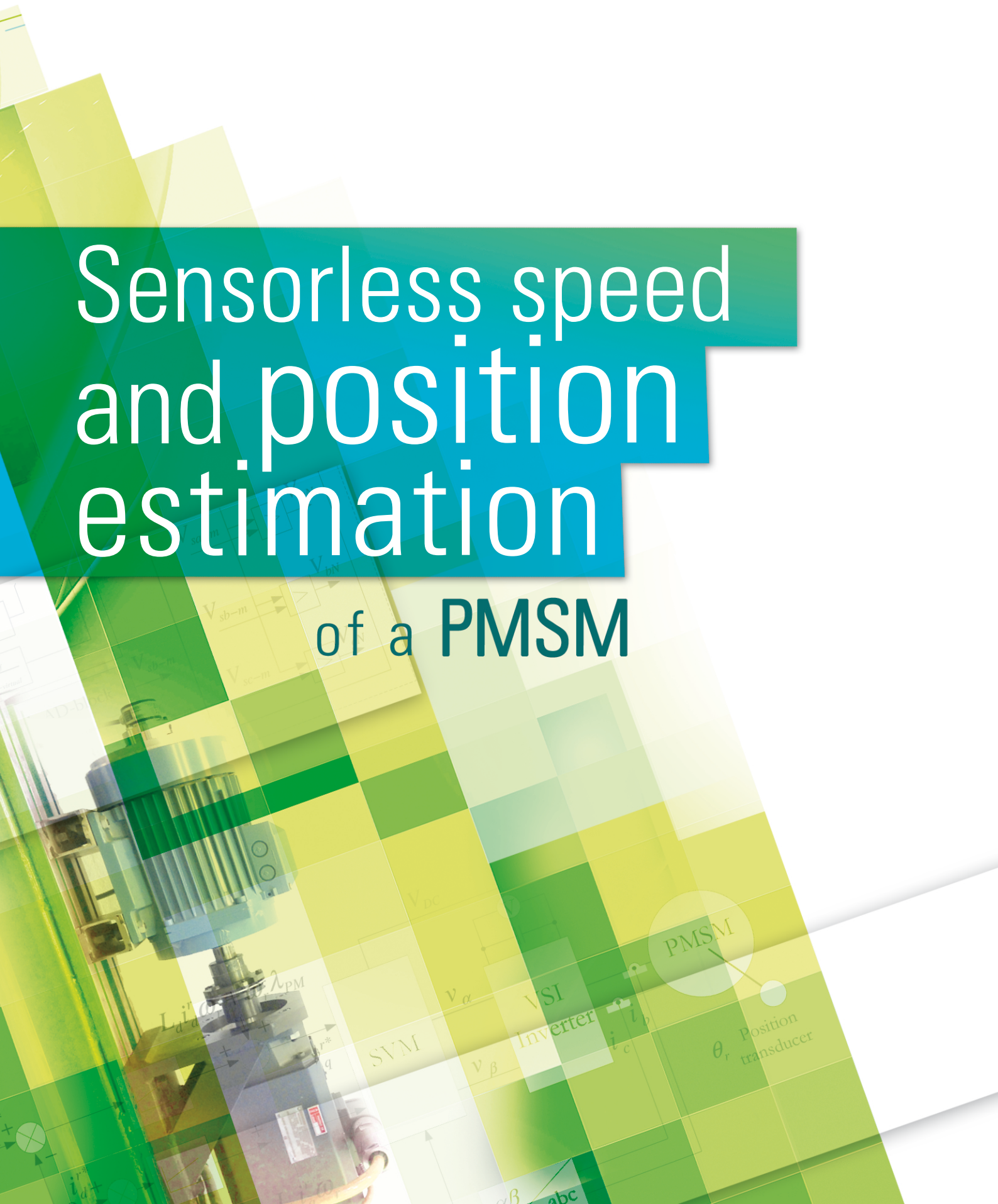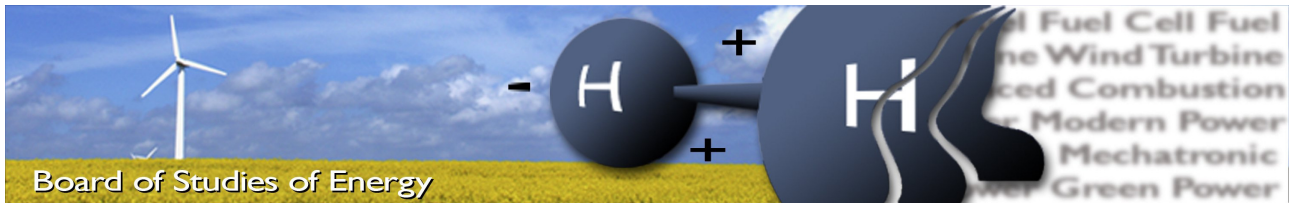Group: PED4-1064
Aalborg University
Department of Energy Technology
June 3, 2014

Sensorless speed and position estimation

of a PMSM

Title:	Sensorless speed and position estimation of a PMSM
Semester:	4rd semester M.Sc., PED4
Semester theme:	Master Thesis
Period:	17-02-2013 / 03-06-2014
ECTS:	30
Supervisor:	Kaiyuan Lu and Hernan Miranda Delpino
Project group:	PED4-1046

Cesar Hernaez

Copies: 2
Number of pages: 75
Appendix pages: 12
CD's: 2

ABSTRACT:

This Project focuses on investigating the sensorless speed and position estimation control of a Surface Mounted Permanent Magnet Synchronous Machine for medium and high speed, proposing a bandwidth for different steady and dynamic states and investigating about the angular estimation position error. Back-EMF method is used to estimate the position, and Phase Loop Lock (PLL) method is used to estimate the speed. An Auto-tuning is designed for both in order to achieve good performance based on the bandwidth and the position error. A field Oriented Control (FOC) system was designed which is know to give good results and good dynamic performance. A VSI controls the machine currents using Space Vector Modulation (SVM). First The literature is searched for a suitable Back-EMF sensorless control method, position error and bandwidth. Then the selected best methods are implemented and tested in the simulation. The overall selected control system is tested in the laboratory setup and compare the sensorless control strategy with the sensored control.

By signing this document, each member of the group confirms that all participated in the project work and thereby that all members are collectively liable for the content of the report.

Table of Contents

List of Symbols

Symbol	Description	Units
f_s	dSPACE system sampling frequency	Hz
f_{sw}	VSI switching frequency	Hz
v_{ab}, v_{bc}, v_{ca}	Line-to-line voltages	V
v_{an}, v_{bn}, v_{cn}	Phase-to-neutral voltages	V
v_{aN}, v_{bN}, v_{cN}	VSI leg voltages	V
S_x	VSI switch state value	–
V_{dc}	VSI DC link voltage	V
$\mathbf{v}_{abcs}$	Stator voltage vector	V
$\mathbf{i}_{abcs}$	Stator current vector	A
$\mathbf{R}_s$	Stator resistance matrix	Ω
$\mathbf{L}_{abcs}$	Stator inductance matrix	H
$\boldsymbol{\lambda}_{abcs}$	Total stator flux linkage	Wb
$\boldsymbol{\lambda}_{pmabcs}$	Permanent magnet flux linkage vector	Wb
v_{qs}^r, v_{ds}^r	q- and d-axis voltages	V
v_α, v_β	α- and β-axis voltages	V
i_{qs}^r, i_{ds}^r	q- and d-axis currents	A
i_α, i_β	α- and β-axis currents	A
L_q, L_d	q- and d-axis inductances	H
L_α, L_β	α- and β-axis inductances	H
λ_α, λ_β	α- and β-axis flux linkage	H
λ_q, λ_d	q- and d-axis flux linkage	H
R_s	Stator resistance	Ω
$\lambda_{\alpha\beta}$	$\alpha\beta$ flux linkage	Wb
λ_{dq}	dq flux linkage	Wb
λ_{pm}	Permanent magnet flux	Wb
θ_r	Electrical angular rotor position	rad
θ	Electrical angular rotor position	rad
ω_r	Electrical angular speed	rad/s
ω	Electrical angular speed	rad/s
θ_m	Mechanical angular rotor position	rad
ω_m	Mechanical angular speed	rad/s
n	Mechanical angular speed	rpm
p_p	Number of polepairs	–
T_e	Electromagnetic torque	Nm
T_{load}	Mechanical load torque	Nm
J_m	Combined inertia coefficient of PMSM and load	kg·m^2
B_m	Combined viscous damping coefficient of PMSM and load	Ns/m
J_0	Combined coulomb friction coefficient of PMSM and load	Nm
n_m	Mechanical shaft speed	min^{-1}
τ	Time constant	s
J_{PMSM}	Inertia coefficient of the PMSM	kg·m^2
J_{IM}	Inertia coefficient of the IM	kg·m^2
$J_{Coupling}$	Inertia coefficient of the coupling	kg·m^2
s	Laplace variable	–

Symbol	Description	Units
K_p	Controller proportional gain	–
K_i	Controller integral gain	–
K_1	Constant gain	–
K_1	Constant gain	–
T_d	DSP system time delay	s
G	Transfer function	–
K_t	Torque constant	Nm/A
T_s	Sampling period	s
e_{ss}	Steady state error	–
T_l	Combined load torque and Coulomb friction	Nm
$\mathbf{f}_{qd0s}$	qd0 variable vector	–
$\mathbf{f}_{abcs}$	abc variable vector	–
$*$	Reference	–
$-$	error	–
$\bar{\theta}_{err}$	Electrical angular error position originate by the saturated inductance	rad
$\bar{\theta}_{ras}$	Electrical angular error position originate by the Rasmussen method	rad
$\hat{\theta}$	Electrical angular estimated position	rad
λ_M	Module of the vector for the electrical angular estimated position	–
H	Magnetic Field Strength	A/m
B	Magnetic field	T
L_a	Artificial inductance	H
L_{anew}	Artificial inductance	H
δ_M	Rassmusen value which have a influence in the error	H
$\hat{\omega}$	electrical speed estimation	rad/s

Abbreviations

Description	Acronym
Alternating Current	AC
Direct Current	DC
Back Electromotive Force	BEMF
Back Electromotive Force	Back-EMF
Internal Model Vontrol	IMC
Kirchhoff's Voltage Law	KVL
Permanent Magnet	PM
Pulse Width Modulation	PWM
Revolution Per Minute	RPM
Permanent Magnet Synchronous Machine	PMSM
Voltage Source Inverter	VSI
Field Oriented Control	FOC
Phase Locked Loop	PLL
Proportional Integrator	PI
Proportional Integrator PLL	PI_{PLL}
Magnetomotive force	MMF
Insulated Gate Bipolar Transistor	IGBT
Space Vector Modulation	SVM
Digital Signal Processor	DSP
Reduced Instruction Set Computer	RISC
Power PC	PPC
Induction Machine	IM
High Pass Filter	HPF
Model Reference Adaptive System	MRAS

Chapter 1

Introduction

1.1 Background

The Permanent Magnet Synchronous Machine (PMSM) has over the recent years become more used in the industries because of their high performance, high efficiency, high torque to inertia ratio, high torque to volume ratio and control properties. PMSM consist of a permanent magnet assembled on the rotor, which will begin rotating due to the interaction with the stator field produced by the three phase current flowing into the windings. The PM rotor follows synchronously the rotating magnetic field generated by the currents. By controlling the frequency and the amplitude current, the magnetic field is controlled, by using Field Oriented Control method (FOC). In FOC, the rotor angular position and speed are needed. It can be obtained in real time with a sensor attached to the rotor shaft, but the sensor increases the machine size, noise interference, total cost and reduces the reliability. Due to this, sensorless control is used instead which calculates rotor position and speed using electrical information measurements. Position estimation based on the Back-EMF sensorless algorithm is one of the best methods when focusing on medium and high speeds.

The motor equations allows for the calculation of the argument of the stator flux linkage vector using the stationary $\alpha\beta$-reference frames.

Back EMF position estimation is made via the reference voltages given by the current controller. The absence of voltage probes reduces the cost of the system and improves its reliability and electromagnetic susceptibility, but introduces an error in the voltage that causes a position error [4]. This problem can be avoided in different ways that provide an under classification estimation position method.

During high current demand the magnetic saturation of the iron core provide to the estimation position an error that can be compensated.

To complete the sensorless control process the speed estimation can be calculated by a Phase-Locked Loop (PLL) basis of the position estimation. The PLL method has been already used successfully to obtain the speed basis of the position.

A good speed estimation depends on the position estimation and the PLL PI controllers. Therefore the study of the response with different Back-EMF position estimation method takes into account the core saturation to remove the position error and the study of the PLL response together with the estimation position, are highly appreciated by the industry.

1.2 Problem statement

This project is focused on the estimation of the speed and the position for medium and high speed range where the Back-EMF estimation position algorithm is used together with a Phase-Locked Loop (PLL).

The main causes that affect this sensorless control method are:

- The drift that appears after the pure integration on the position estimation Back-EMF equations.
- The position error.
- The position and the speed estimation bandwidth.

The drift can be originate from the inaccurate parameters machine measured that can cause a voltage error, and because of a small drift in the current [10].

High current demand causes the saturation PMSM core to create an error in the estimation position.

Bad bandwidth choices can cause problems in the response and even to do the system unstable.

1.3 Objective

The objective of this project is to design and implement, both in the simulations and in an experimental set up, a sensorless algorithm to control a surface mounted PMSM using FOC considering the inductance saturation making a compensation of it in order to reduce the position error that is produced. After selecting the sensorless method that best fits our requirements, an efficient tuning method should be proposed in order to find the best bandwidth of the rotor speed and position algorithm during the different conditions. The sensorless control influence should be reconsidered for the speed close loop.

After running the entire model using Matlab and Simulink it will be introduced using dSPACE real time interface in the laboratory in order to test the reliability of the theoretical study.

1.4 Limitations and assumptions

In reality, the set up is not exactly the same as in the simulations, and therefore some limitations and assumptions are considered during the preparation and development of this project.

PMSM model:
- The stator windings produce sinusoidal MMF distribution in the air-gap.
- The supply voltages are symmetrically balanced.
- The increasing of the resistance produced by the temperature are neglected.
- The losses of the reactance produced by the conductions wires are neglected.
- The mechanical system is modeled as a one-mass system, thereby neglecting any elasticity in the coupling.

VSI model:
- The switches in the VSI model are implemented with dead time of 2.5 μs.
- The switching frequency of the VSI is fixed to 5 kHz.

Rotor Position and speed stimate:
- Mediumtohighspeedrange of the SMPMSM is considered.

dSPACE laboratory setup:
- The dSPACE system sampling frequency is fixed to 5 kHz.
- The encoder mounted in the shaft, is in the back part of the PMSM.

Chapter 2

System Description

This chapter presents an overview of the system where the dSPACE is used in order to perform the control of the PMSM. Field Oriented control technique is implemented jointly with sensorless control. Mathematical Equations of the inverter and the PMSM are presented, which are applied to the simulation model using MATLAB/Simulink.

2.1 System overview

In this project the Permanent Magnet Synchronous Machine is assembled in the same shaft with the Induction Machine with the purpose of obtaining a load in the system. Both machines are controlled by two inverters which are fed by a DC voltage. A PMSM and a IM are fed by two voltage source inverters (VSI). The VSI controls the machine currents using Space Vector Modulation (SVM). The inverters are controlled by the PC using dSPACE software. At the same time, it is manipulated utilizing MATLAB/Simulink.
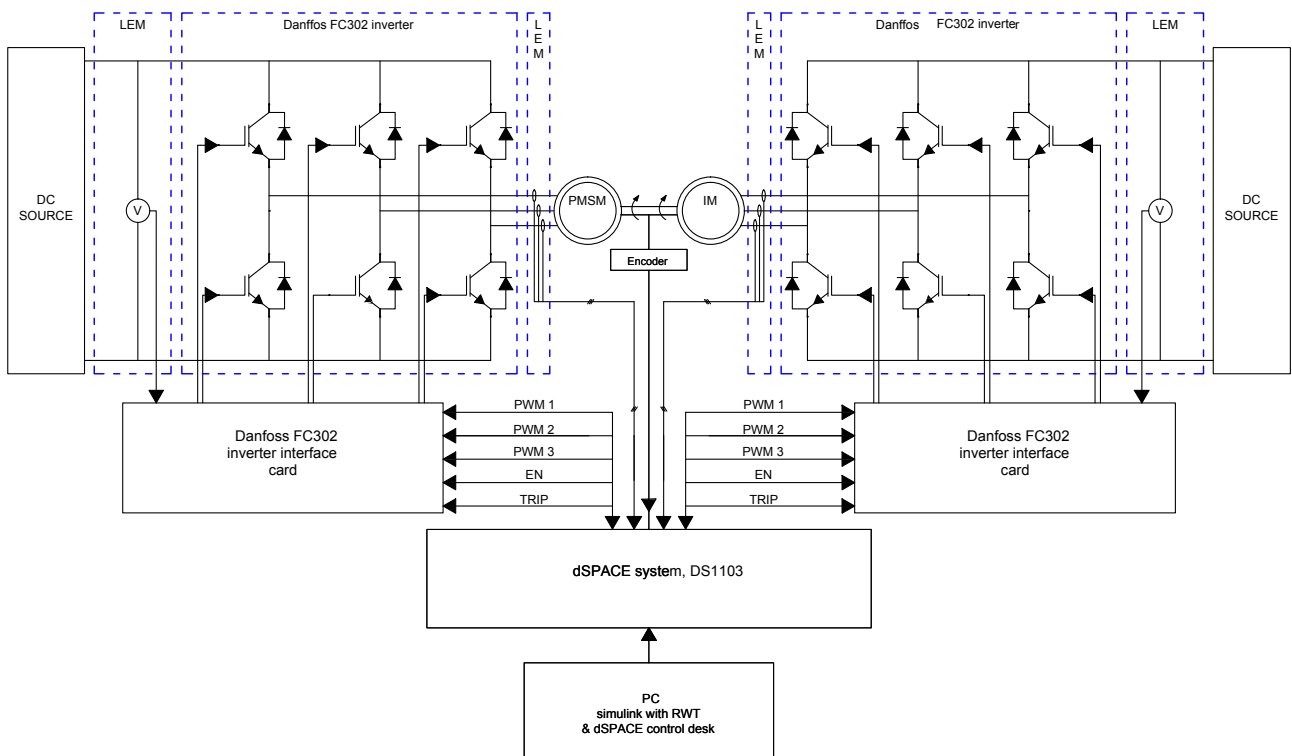

Figure 2.1. Overview of the drive system [6].

Figure 2.1 shows an overview of the drive system.
Voltage and current values are measured by the LEM modules and the rotor position is measured on the encoder to compare results from different sensor-less experiments.

2.1.1 System parameters

In Table 2.1 the datasheet specifications of the PMSM are shown.

Table 2.1. Siemens PMSM type ROTEC 1FT6084-8SH7 [1]

Description	Parameter	Value
Rated power	P_{rated}	9.4 kW
Rated current	I_{rated}	24.5 A
Rated frequency	f_{rated}	300 Hz
Rated speed	n_{rated}	4500 min^{-1}
Rated torque	T_{rated}	20 Nm
Inertia constant	J_{PMSM}	0.0048 kg· m^2
Stator resistance	R_s	0.18 Ω
d-axis inductance	L_d	2 mH
q-axis inductance	L_q	2 mH
PM flux-linkage	λ_{pm}	0.123 Wb
Pole pairs (poles)	Pp	4

The Resistance, Inductance and the flux-linkage parameters are measured experimentally for the machine that is used in the project. It is known that the manufacturer parameter values are equal for all machines of the same type [6]. For that the values measured are considered more accurate and therefore are the ones implemented in the simulations. In Table 2.2 the PMSM parameters and manufacturer parameters are compared.

Table 2.2. Comparison of the PMSM manufacturer parameters and the obtained laboratory parameters.[1]

Description	Parameter	Manufacturer value	Lab. value	Rel. deviation
Stator resistance	R_s	0.18 Ω	0.19 Ω	5.55 %
d-axis inductance	L_d	2 mH	2.2 mH	10 %
q-axis inductance	L_q	2 mH	2.2 mH	10 %
PM flux-linkage	λ_{pm}	0.123 Wb	0.12258 Wb	0.4 %

As was mentioned before, the PMSM is coupled with an IM. The IM inertia PMSM inertia and the coupling inertia are taken into account. The values of the inertia are listed in Table 2.3 [6]

Table 2.3. Manufacturer inertia values for the dSPACE setup system.

Component	Parameter	Inertia [kg· m^2]
IM	J_{IM}	0.0069
PMSM	J_{PMSM}	0.0048
Coupling	$J_{Coupling}$	0.0029
Total		0.0146

The total inertia J_m (2.1), is the combined moment of inertia used in the setup.

$$J_m = J_{PMSM} + J_{IM} + J_{Coupling} \qquad \left[\text{kg} \cdot \text{m}^2 \right] \tag{2.1}$$

After all, the Table 2.4 shows the values used on the simulations of the model and designed through MATLAB/Simulink.

Table 2.4. Determined dSPACE setup system parameters.

System	Description	Parameter	Value
PMSM	Stator resistance	R_s	0.19 Ω
	d-axis inductance	L_d	2.2 mH
	q-axis inductance	L_q	2.2 mH
	PM flux-linkage	λ_{pm}	0.12258 Wb
Mechanical	Inertia	J_m	0.0146 kg·m^2
	Coulomb friction	J_0	0.2295 Nm
	Damping	B_m	0.0016655 Ns/m
VSI and dSPACE	Switching frequency	f_{sw}	5000 Hz

A dead-time is implemented with the goal of protecting the IGBTs. If two of them are turned on at the same time on the same leg, they will be damaged due to a short circuit causing the whole system to defect. The dead-time for the inverter is 2.5 μs. The dead-time, IGBT voltage drop and turn on/turn off time causes a voltage error at the inverter output signal [21].

2.2 PMSM mathematical model

The Permanent Magnet Synchronous Machine(PMSM)is a Siemens PMSM type ROTEC 1FT6084-8SH7. It is controlled by the inverter that provides the specific values demanded by the control. The datasheet specifications of the PMSM are listed in the Table 2.1.

In this chapter, the mathematical equations of the PMSM in dq or rotor fixed reference frame model are presented. The equations (2.2), (2.3), (2.4), (2.5), (2.6), and (2.7) are the result of the developed model that takes into account the complete physical model. It includes an electrical and mechanical model system. These equations are implemented on the computer simulations by using the proper adjustment and appropriate machine parameters.

The following Figure 2.2 shows equivalent circuit for the synchronous machine with a non-salient rotor in dq reference frame.
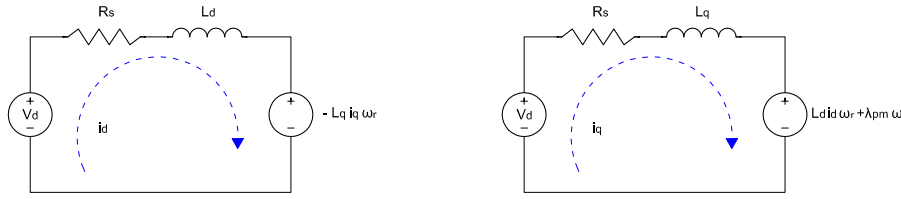
Figure 2.2. Equivalent circuit for the synchronous machine.

Voltage equation can be easily calculated observing the equivalent circuit using the Kirchhoff's voltage law (KVL).

$$(2.2) \qquad v_{qs}^r = R_s i_{qs}^r + \omega_r (L_d i_{ds}^r + \lambda_{pm}) + L_q \frac{d}{dt} i_{qs}^r \qquad \text{[V]}$$

$$(2.3) \qquad v_{ds}^r = R_s i_{ds}^r - \omega_r L_q i_{qs}^r + L_d \frac{d}{dt} i_{ds}^r \qquad \text{[V]}$$

The electrical torque produced by the motor is described by the following equation:

$$(2.4) \qquad T_e = \frac{3}{2} p_p \left[\lambda_{pm} + (L_d - L_q) i_{ds}^r \right] i_{qs}^r \qquad \text{[Nm]}$$

Mechanical and electrical torque produced by the motor are related by the following equation:

$$(2.5) \qquad T_e = T_{load} + B_m \omega_m + J_0 + (J_m) \frac{d}{dt} \omega_m \qquad \text{[Nm]}$$

When the angular position is known, the angular speed can be calculated:

$$(2.6) \qquad \omega_r = \frac{d}{dt} \theta_r \qquad \text{[rad/s]}$$

Mechanical angular velocity ω_m and electrical angular velocity ω_r are related by the pair of poles (p_p).

$$(2.7) \qquad \omega_r = p_p \omega_m \qquad \text{[rad/s]}$$

2.3 Inverter

In the dSPACE setup, the inverter is connected to a DC supply. It is a Danfoss FC302 full bridge Voltage Source Inverter that consists of 6 semiconductor IGBTs positioned in three legs.

Figure 2.3 shows the inverter schematic where each IGBT is considered as an ideal switch. The load impedances, Y-connected, represents the PMSM.

The objective of the inverter is to convert the DC voltage provided by the DC link into a specific AC voltage. The AC voltage demanded by the control system is supplied by the inverter.
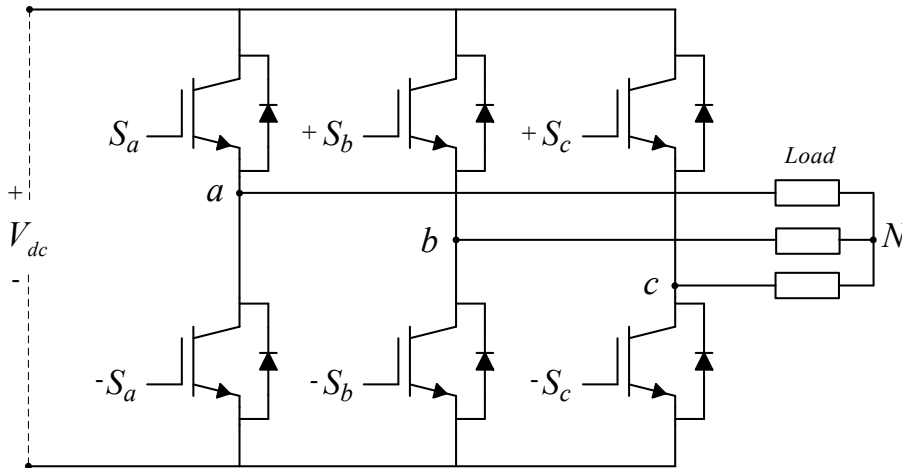
Figure 2.3. Topology of the IGBT Voltage Source Inverter [6].

The variable S is introduced in order to determinate the switching status. S has value 1 when upper leg semiconductor is on and 0 when it is off. S_a, S_b and S_c correspond to the states of leg_a, leg_b and leg_c respectively. As was mentioned before two transistors on the same inverter leg can not be turned on at the same time, therefore 8 different switching stages can be applied, where two of those are zero voltages which are (111) and (000).
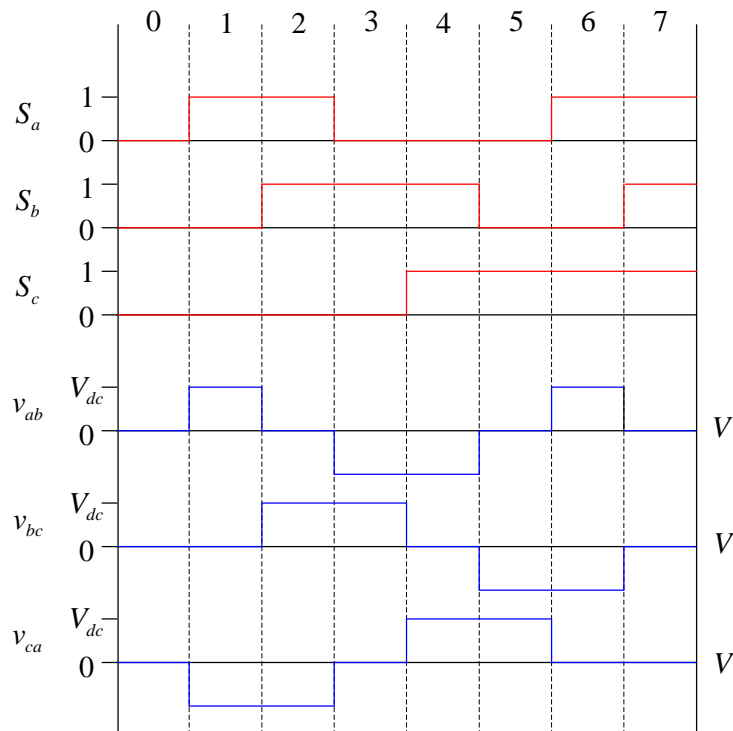

Figure 2.4. Switching functions and the resulting output line-to-line voltages from a full bridge inverter [6].

The line-to-line voltages as a function of the switch states are given by (2.8).

(2.8)
$$\begin{bmatrix} v_{ab} \\ v_{bc} \\ v_{ca} \end{bmatrix} = V_{dc} \begin{bmatrix} 1 & -1 & 0 \\ 0 & 1 & -1 \\ -1 & 0 & 1 \end{bmatrix} \begin{bmatrix} S_a \\ S_b \\ S_c \end{bmatrix}$$
[V]

And the line-to-neutral voltages as a function of the switch states are given by (A.5).

(2.9)
$$\begin{bmatrix} v_{aN} \\ v_{bN} \\ v_{cN} \end{bmatrix} = \frac{V_{dc}}{3} \begin{bmatrix} 2 & -1 & -1 \\ -1 & 2 & -1 \\ -1 & -1 & 2 \end{bmatrix} \begin{bmatrix} S_a \\ S_b \\ S_c \end{bmatrix}$$
[V]

Chapter 3

FOC control

3.1 Introduction

In this chapter the description of the FOC is presented. This method is done by making proper simplifications and tuning the PI controls parameters in the current and speed close loops.

3.2 FOC Strategy

The control can be divided into two main groups, scalar and vector control. Scalar control is based on control of both magnitude and frequency of the stator voltage or of the stator current, maintaining a constant ratio voltage/frequency. However, this type of control is just valid in a steady state. Vector control is primarily implemented because it is applicable to dynamics states. Instantaneous position of voltage, current and flux space vectors are controlled. Thus, the control system achieves the position of the space vectors and guarantees their correct orientation for both steady states and transients [8].

Field Oriented Control is one of the most popular methods because it enables the PMSM to achieve a high performance level. Since the electrical torque produced by the machine is just a function of the i_q current (3.1), the current is maintained on the d axis and maximum torque per ampere is achieved. Therefore the copper losses are minimized and the maximum efficiency is obtained.

$$(3.1) \qquad T_e = \frac{3}{2} \cdot p_p \cdot (\lambda_{pm} \cdot i_q) \qquad \text{[Nm]}$$

The angle of the vector between the flux produced by the stator and the permanent magnet flux is kept constant. It is for this reason that this control is also called constant torque angle strategy(CTA). It is one of the easier strategies and most widely used in the industry [8].

The stator flux is produced by i_q stator current so the torque depends on the permanent magnet flux and i_q. The goal is to constantly maintain ninety electrical degrees between the current space vector and the flux axis caused by the rotor permanent magnet [18].

In (3.2), the three stator currents in the abc frame are shown taking the torque angle (δ) into account .

$$(3.2) \qquad \begin{bmatrix} i_{as} \\ i_{bs} \\ i_{cs} \end{bmatrix} = i_s \begin{bmatrix} \cos(\theta_r + \delta) \\ \cos(\theta_r + \delta - 120°) \\ \cos(\theta_r + \delta + 120°) \end{bmatrix} \qquad \text{[A]}$$

θ_r is the electrical rotor position, and δ is the angle between the rotor field and the stator current phasor that produces the stator flux.

The three stator currents in abc frame are transformed in dq reference frame, as it is shown in the following equation (3.3).

$$(3.3) \quad \begin{bmatrix} i_{ds}^r \\ i_{qs}^r \end{bmatrix} = \frac{2}{3} \begin{bmatrix} \cos(\theta_r) & \cos(\theta_r - 120°) & \cos(\theta_r + 120°) \\ \sin(\theta_r) & \sin(\theta_r - 120°) & \sin(\theta_r + 120°) \end{bmatrix} \begin{bmatrix} i_{as} \\ i_{bs} \\ i_{cs} \end{bmatrix} = i_s \begin{bmatrix} \cos(\delta) \\ \sin(\delta) \end{bmatrix} \qquad [\text{A}]$$

In Figure 3.1 the angle δ and θ_r are represented in dq-reference frame.
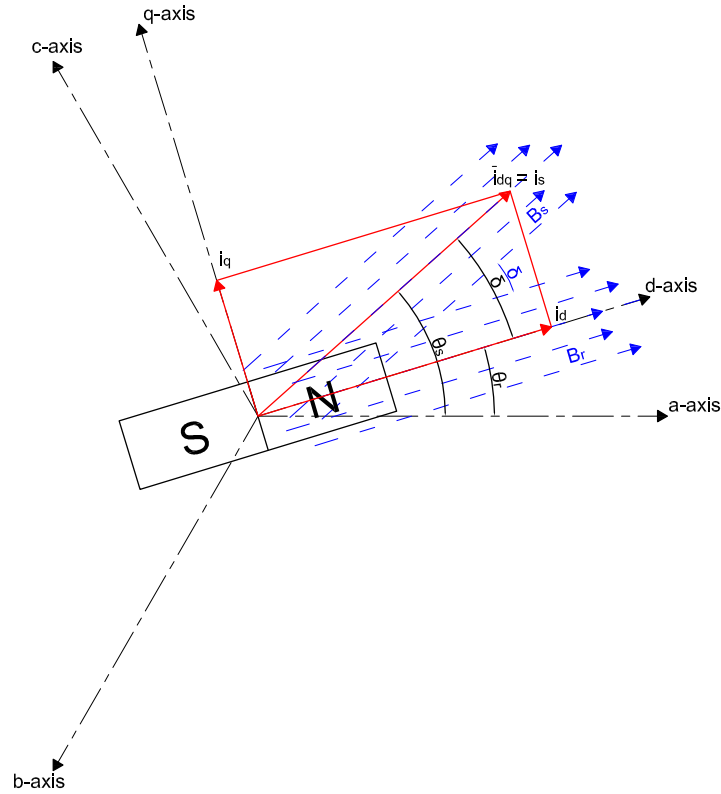
Figure 3.1. Vector diagram used to represent the PMSM and current vector and flux [6].

3.3 Control design

3.3.1 Decoupling control

In order to simplify the control of the PMSM, a compensation method is applied decoupling the BEMF.

The voltage equations of the motor as shown above in the mathematical model 2.3 and 2.2 are obtained in the Laplace domain as is shown in the equations 3.4 and 3.5.

$$(3.4) \qquad V_{ds}^r(s) = R_s + L_d s I_{ds}^r(s) - \omega_r \left(L_q I_{qs}^r(s) \right) \qquad \text{[V]}$$

$$(3.5) \qquad V_{qs}^r(s) = R_s + L_q s I_{qs}^r(s) + \omega_r \left(\lambda_{pm} + L_d I_{ds}^r(s) \right) \qquad \text{[V]}$$

BEMF can be decoupling knowing the terms: λ_{pm}, L_q, L_d, i_{qs}^r, i_{ds}^r and ω_r. This is illustrated in 3.2 where the Physical model of the PMSM contains the mutual coupling and the control system contains the decoupling.
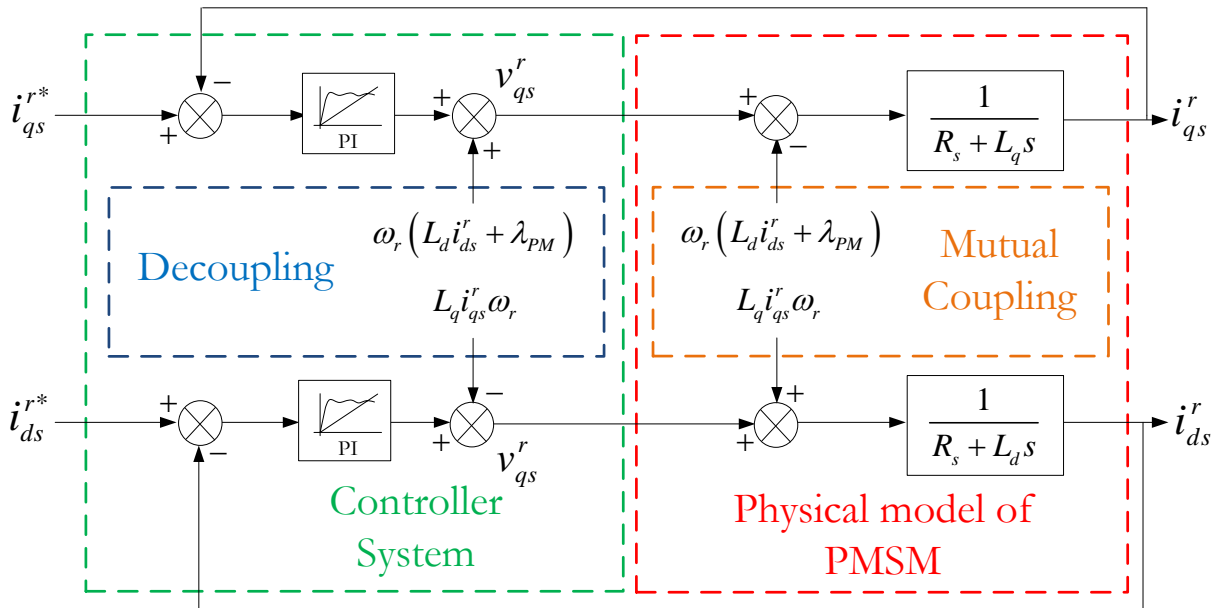

Figure 3.2. Decoupling of the d- and q-axis Back-EMF disturbances [1].

By decoupling the BEMF disturbances the transfer functions of the plants in Laplace domain are shown in (3.8) and (3.6)below.

As shown in equation (3.1) the electromagnetic torque has a linear relationship with the current displayed, therefore the electromagnetic torque is controlled by controlling the current.

Since the output is the voltage and the input is the current: $I_{qs}^r(s) \, / \, V_{qs}^r(s)$ and $I_{ds}^r(s) \, / \, V_{ds}^r(s)$. The transfer functions are shown in the equations 3.6 and 3.8 after the BEMF disturbance is decoupled.

$$(3.6) \qquad \frac{I_{ds}^r(s)}{V_{ds}^r(s)} = \frac{1}{R_s + L_d s} \qquad\qquad [\text{A/V}]$$

$$(3.7) \qquad \frac{I_{qs}^r(s)}{V_{qs}^r(s)} = \frac{1}{R_s + L_q s} \qquad\qquad [\text{A/V}]$$

The control is illustrated in the figure 3.3 where three close loops are needed:

- Two inner current control loops that control the torque are shown in the equation 3.1 where i_d command zero current, in order to achieve the goal of the FOC, and i_q depends on the requirements of the system.

- An outer speed control loop.

Figure 3.3. General scheme of Field Oriented Control.

PI controllers are implemented in each loop which are necessary to archive the requirements of the system.

The transformations of the reference frames are possible because the shaft position is determined by the sensor. The DC voltage provided by the DC-link is measured in order to feed the space vector modulation (SVM) that generate the signals that controls the voltage switch inverter (VSI).

The requirements for the FOC control system can be stated as [1]:

- The overshoot should be lower than 5% for the current loop.

- The overshoot should be lower than 25% for the speed loop.

- The risetime for the current loops should be in the proximity of 2 ms.

- The speed loop should be at least ten times slower than the current loop.

After all the requirements of the system are presented that will be achieved by tuning the PI controllers into each loop that are divided into two controls because the two inner current loops have the same PI control values. Therefore in the next chapter the current loop control and the speed control will be presented.

3.3.2 Current loop

Since the L_d and L_q are the same, control of both i_q and i_d will be the same, so only one current loop is presented.

The close loop structure system 3.4 shows the PMSM plant with the PI controller and the two delays produced by the dSPACE.

The delays are introduced in the system by the dSPACE system Digital Signal Processor (DSP):

- The delay introduced to the digital calculation, where the T_s is the sampled period produced by the switching frequency where $T_s = 1/f_s$ since $f_s = f_{sw}$=5000Hz [8].

- The delay introduced by the digital to analog conversion that introduces a time constant of 50% of T_s which is placed in the feedback of the transfer function.
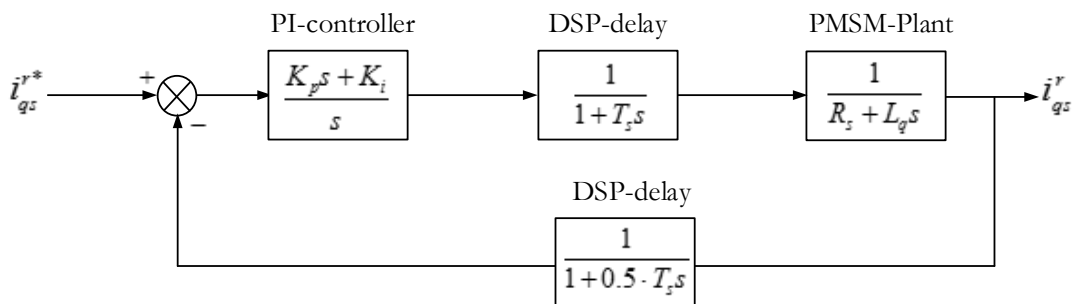
Figure 3.4. q-axis current loop with delays introduced by the dSPACE system.

The delay placed in the feedback is moved in order to work with a unitary feedback 3.5.
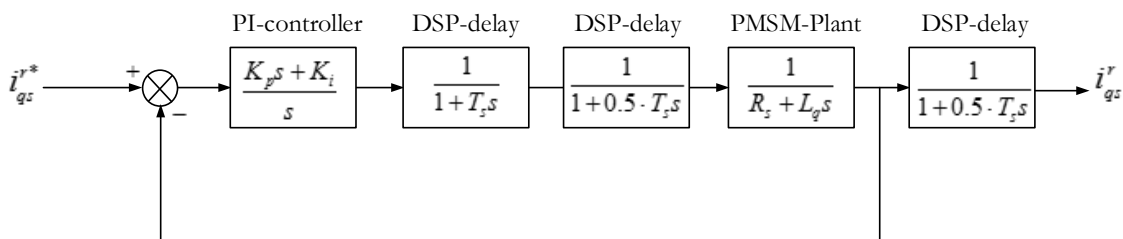
Figure 3.5. q-axis current loop when delays, introduced by the dSPACE, is moved.

A simplification in the transfer function can be made, introducing the time constant T_d which is the sum of all the time constants delays. It can be performed because their values are really small compared with the time constant introduced by the PMSM-Plant. The transfer function of the delays will be replaced by a unique transfer function, making an approximation.

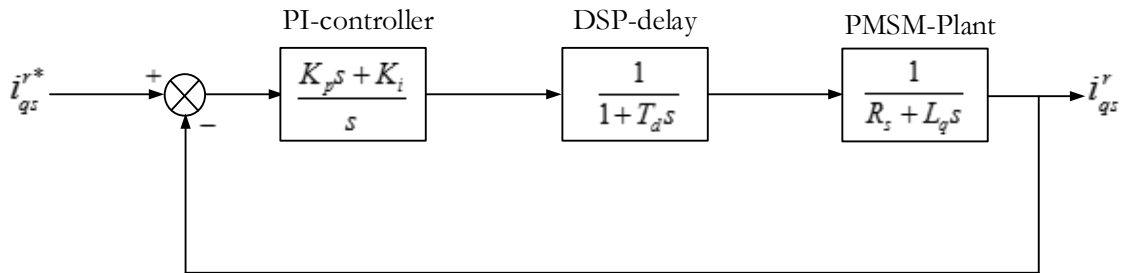$$(3.8) \qquad\qquad T_d = T_s + 0.5 \cdot T_s \qquad\qquad [\text{s}]$$

PI-controller   DSP-delay   PMSM-Plant

Figure 3.6. Simplification of the q-axis current loop with delays introduced by the dSPACE system.

The Integral and the Proportional values of the PI controllers should be chosen according to the requirements set out above. This can be done by applying Internal Model Control (IMC). Then K_i and K_p are calculated.

The plant transfer function is determined after the decoupling is removed from the voltage equation where the current is the input and the voltage is the output 3.9. As mentioned before, the control is performed just for i_q since for i_d the value will be the same.

$$(3.9) \qquad\qquad G_p(s) = \frac{1}{R_s + L_q s} = \frac{\frac{1}{R_s}}{1 + \frac{L_q}{R_s} s} = \frac{K}{1 + \tau s}$$

Where the τ is the time constant and K is a constant value that corresponds with the inverse of the stator resistance.

$$(3.10) \qquad\qquad \tau = \frac{L_q}{R_s}, \quad K = \frac{1}{R_s}$$

Calculating the inverse of the plant,

$$(3.11) \qquad\qquad \frac{1}{G_p(s)} = \frac{1 + \tau s}{K}$$

implementing a filter transfer function,

$$(3.12) \qquad\qquad C(s) = \frac{1}{G_p(s)} f(s)$$

and selecting a first order system filter

(3.13)
$$f(s) = \frac{1}{1 + \lambda s}$$

gives:

(3.14)
$$C(s) = \frac{1}{\left(\frac{K}{\tau s + 1}\right)} \cdot \frac{1}{\lambda s + 1} = \frac{\tau s + 1}{K \cdot (\lambda s + 1)}$$

With $C(s)$ and $G_p(s)$, the equivalent PI controller is obtained using the following equation 3.16.

(3.15)
$$G_{PI}(s) = \frac{C}{1 - CG_p} = \frac{\frac{\tau s + 1}{K \cdot (\lambda s + 1)}}{1 - \left(\frac{K}{\tau s + 1}\right) \cdot \left(\frac{\tau s + 1}{K \cdot (\lambda s + 1)}\right)} = \frac{\frac{1}{K} \cdot \frac{\tau s + 1}{(\lambda s + 1)}}{\frac{(\lambda s + 1) - 1}{\lambda s + 1}} = \frac{\tau s + 1}{K \cdot \lambda s}$$

(3.16)
$$= \frac{1}{K \cdot \lambda}\left(\tau + \frac{1}{s}\right) = \frac{\tau}{K \cdot \lambda} + \frac{1}{K \cdot \lambda} \cdot \frac{1}{s} = K_p + K_i \cdot \frac{1}{s}$$

Knowing the constant value K and the time constant τ, allows for the calculation of K_i and K_p using the equations (3.9) and 3.17.

(3.17)
$$K_i = \frac{1}{K \cdot \lambda} = \frac{1}{\frac{1}{R_s} \cdot \lambda} = R_s \cdot \frac{1}{\lambda}$$

$$K_p = \frac{\tau}{K \cdot \lambda} = \frac{\frac{L_q}{R_s}}{\frac{1}{R_s} \cdot \lambda} = L_q \cdot \frac{1}{\lambda}$$

λ drives the current response system because it directly affects the controller gain. This means that using small values of λ results in a faster closed-loop response and vice versa [3].

According to the previously defined response requirements for the FOC, the value of λ is calculated, due to the requirements, the response should be fast. So the IMC λ is assigned a small value ($\lambda = 0.00088$). After λ is selected the values of the PI controller are obtained by using equation 3.18.

(3.18)
$$K_i = R_s \cdot \frac{1}{\lambda} = 0.19 \cdot \frac{1}{8.8 \cdot 10^{-4}} = 215.9 \ , \quad K_p = L_q \cdot \frac{1}{\lambda} = 0.0022 \cdot \frac{1}{8.8 \cdot 10^{-4}} = 2.5$$

In order to fully fit to the requirements of the system the values of the PI controller are: $K_{qi} = K_{di} = 135$ and $K_{qp} = K_{qp} = 2.5$.

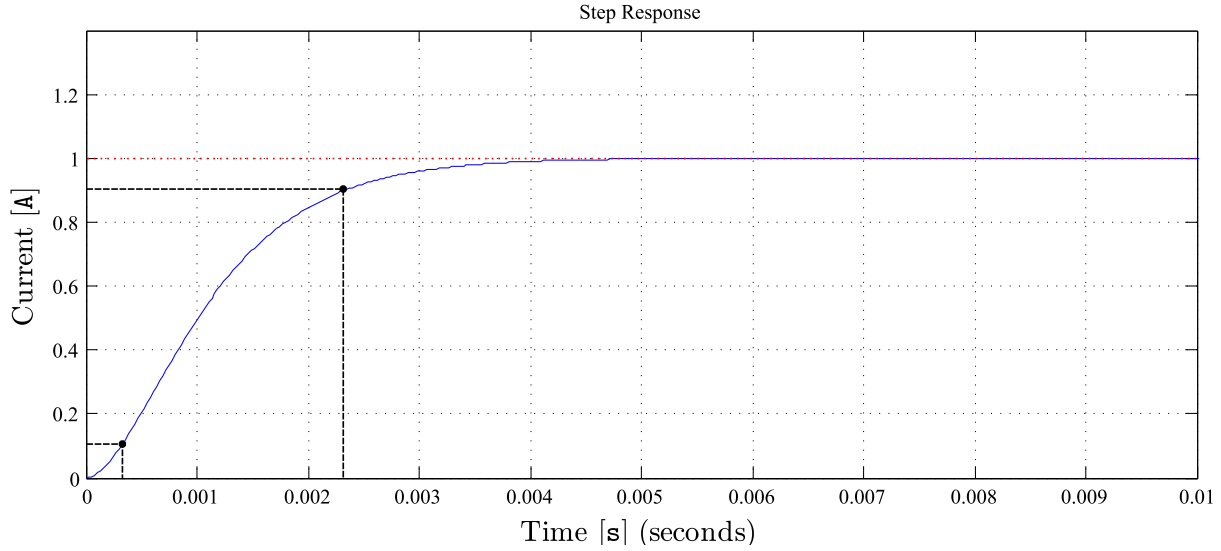The close loop response of the current close-loop transfer function is shown in the figure 3.7.

Figure 3.7. Unit step q-axis current close loop with delays.

Where the values obtained from the response are considered sufficiently acceptable as they meet the requirements.

- Rise Time: 0.0020 [s]
- Settling Time: 0.0035 [s]

3.3.3 Speed loop

The control is present just using i_qc current loop, knowing that the control of the torque is related just with the current i_q. The transfer function for control of the speed is obtained from the following equations 3.19, 3.20.

$$T_e = \frac{3}{2}p_p(\lambda_{pm} \cdot i_q) \qquad \text{[Nm]} \tag{3.19}$$

$$T_e = T_{load} + B_m\omega_m + J_0 + (J_m)\frac{d}{dt}\omega_m \qquad \text{[Nm]} \tag{3.20}$$

where it can be noticed that the torque is proportional to the current 3.21 and is considered as a transfer function.

$$G_T(s) = \frac{T_e}{i_{qs}^r} = \frac{3}{2}p_p\lambda_{pm} = K_t \qquad \tag{3.21}$$

The coulomb friction is added to the load 3.22 into a new value T_l.

$$T_l = T_{load} + J_0 \qquad \text{[Nm]} \tag{3.22}$$

The connection between the electrical torque and the mechanical speed is found in the equation in relation with the current. Therefore the plant of the speed transfer function of the speed is represented where the input is the electrical Torque and the output is the speed where T_l is considered zero.

$$(3.23) \qquad G_\omega(s) = \left.\frac{\omega_m}{T_e}\right|_{T_l=0} = \frac{1}{J_m s + B_m}$$

In the Figure 3.10 the outer speed loop of the system is illustrated with the current plant, the DSP delays, which should be also considered like in the current control, the PI control that is needed to achieve the requirements of the system, the Torque constant and the current plant, that is the inner close loop already tuned.
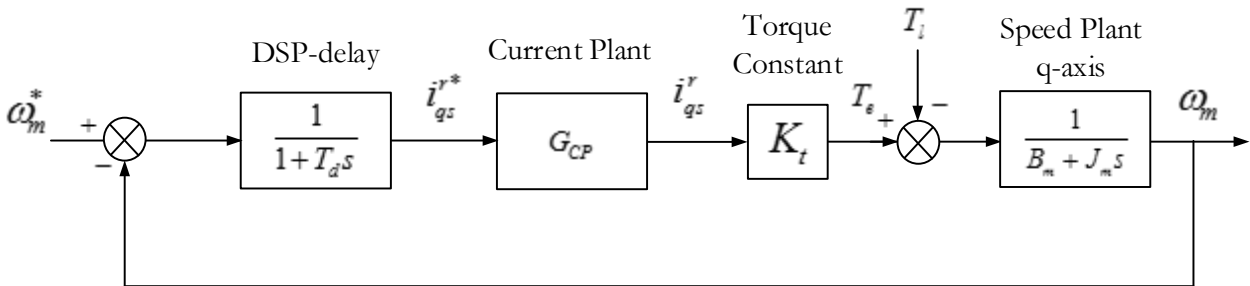
Figure 3.8. Speed loop with delays and the current close loop transfer functions, without PI controllers.

Because the damping ratio value is really small, the transfer function of the speed plant can be considered like a free integrator and therefore the steady state error of the close loop speed system is imperceptible, affected only by K_t. Therefore the system can be controlled with a proportional, when $T_l=0$. It is shown in the figure 3.9 (top left graph). The figure shows also that the system is stable without speed PI controller, verified by the rood locus where the poles of the system are located in the left-half plane (LHP).
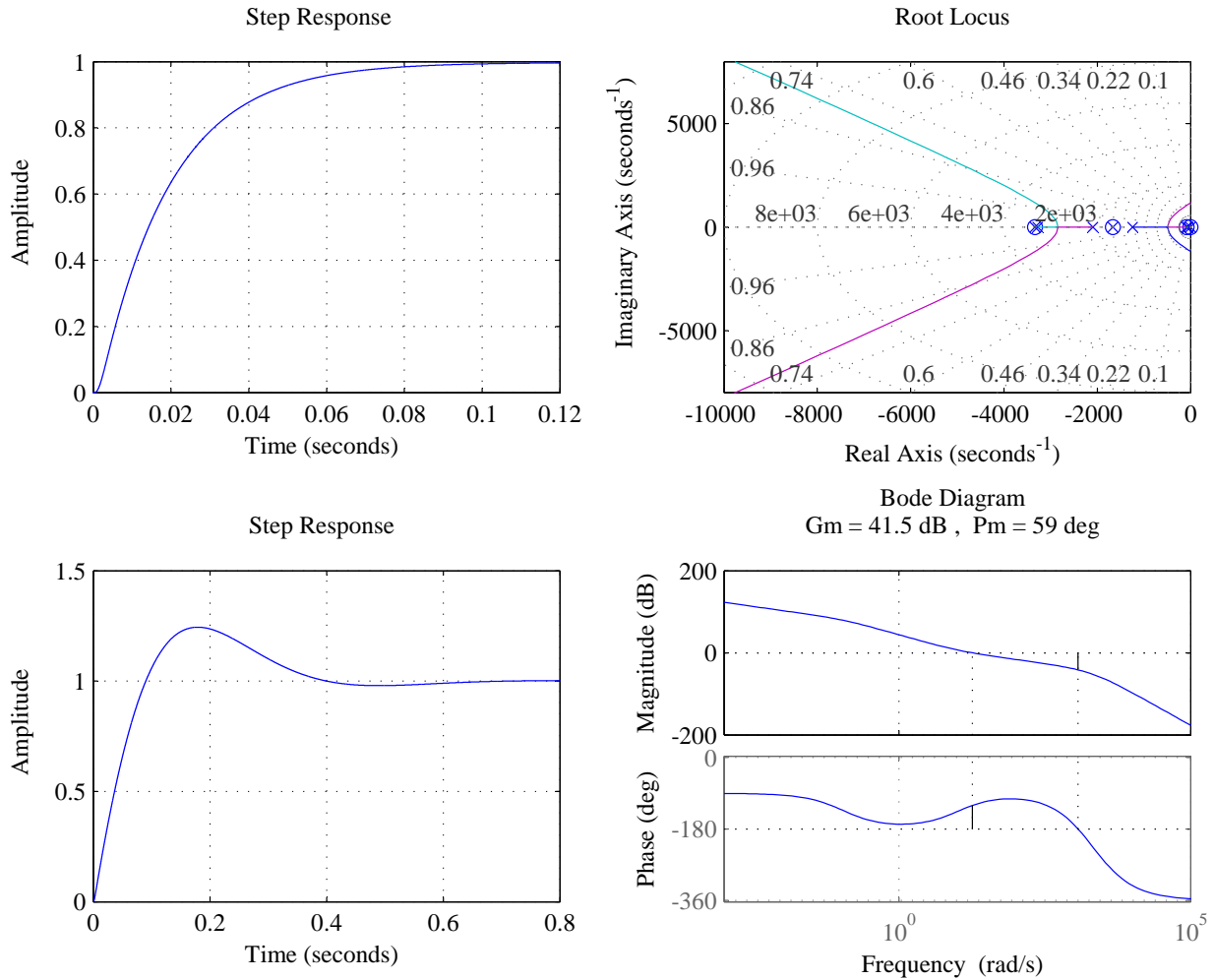
Figure 3.9. Speed controller: root locus (without PI controllers), open loop bode diagram (with PI controllers), unit step (with and without PI controllers).

However the system has to support a load T_l, which requires a control with a PI controller that should be introduced. The steady state error produced by the system depends on the constant gain K_t and the load disturbance, since $T_l \neq 0$.

$$(3.24) \qquad\qquad e_{ss} = \omega_m^* - \frac{T_l}{K_t}$$

The PI controller is therefore introduced in the system to eliminate the steady state error.
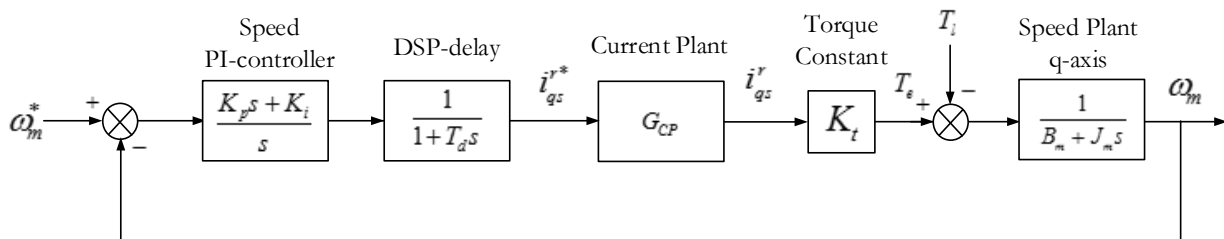
Figure 3.10. Speed loop with delays and the current close loop transfer functions, with PI controllers.

(3.25)
$$G_c\left(s\right) = \frac{K_p s + K_i}{s} = K_p\left(1 + \frac{1}{T_i \cdot s}\right)$$

The proportional gain of the PI controller is tuned until it becomes fast enough to fulfill the requirements and then the integral is adjusted until a phase margin of 40° - 60° degrees is reached (no disturbance) [15]. The bode plot with the gain margin is show in the figure 3.9.

(3.26)
$$G_c\left(s\right) = \frac{0.3s + 3.2}{s}$$

The response of system with the tuned parameters is shown in figure 3.9 (bottom left graph).
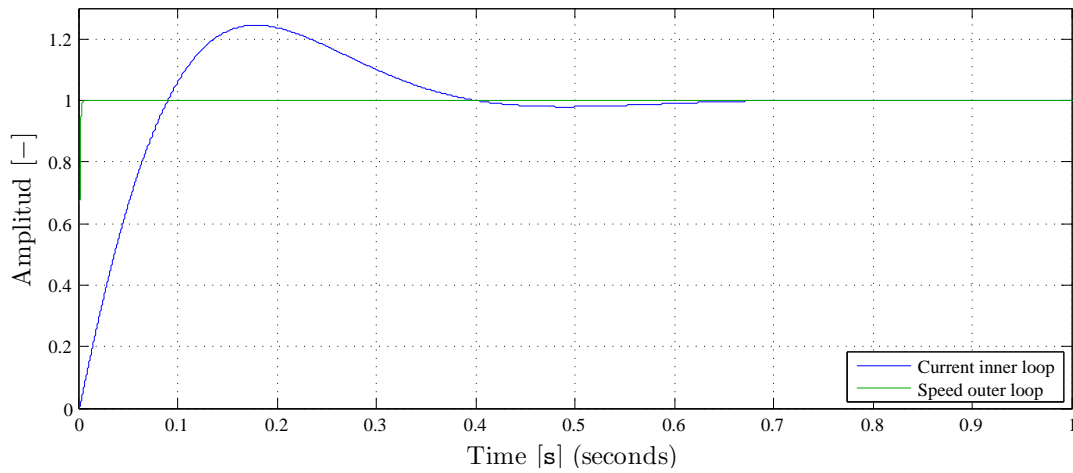
Figure 3.11. Current and speed close loop unit step response.

Finally the steps response of both, inner current close loop and outer speed close loop, are shown together in the same graph 3.11, with the characteristics that archive the requirements for the FOC.

Characteristics of the outer speed close loop step response:

- Rise Time: 0.0682 [s]
- Settling Time: 0.5106 [s]
- Overshoot: 24.4254 %

Characteristics of the inner current close loop step response:

- Rise Time: 0.0020 [s]
- Settling Time: 0.0035 [s]

3.3.4 Anti windup

When the control of the current speed was designed, the limits of the system were ignored, however, in reality there are limits. The voltage that is controlled by the inverter is fixed by the DC-link which produces a limit in the current.

When high values of speed and torque are commanded, the limits are exceeded. In order to not exceed these limits, the system is provided by a saturation block. The problem is that although this limit is regulated by the saturation block, the machine will remain at the maximum limit, as shown in the figure 3.13, for a long time due to the demands of the system. This reduces the time which the output is at the saturation limit, reducing the damage to the machine and increasing its reliability [6].

In order to solve this problem an anti windup is introduced, so the limits will be respected and the maximum limit will not remain for a long time and the response will be better as seen in the figure 3.13.

Figure 3.12 shows the PI controller structure with anti windup scheme [9].
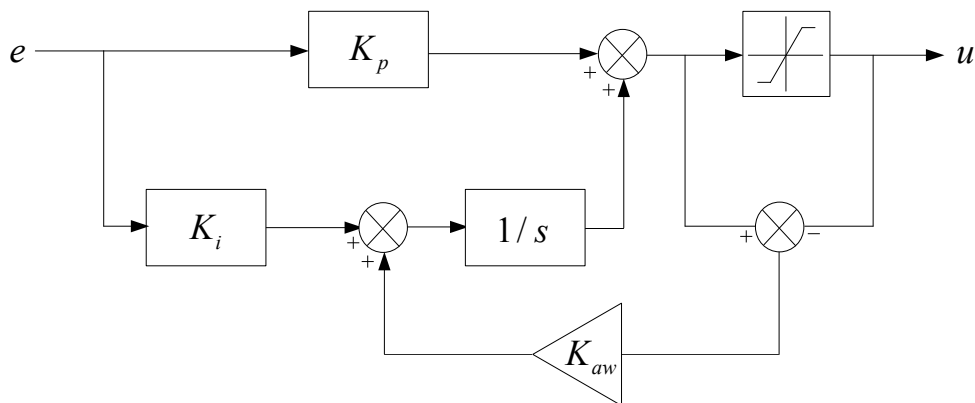
Figure 3.12. PI controller structure with anti windup scheme [6].

It introduces a gain K_{aw} that increase the integral gain. Knowing that increasing the integral gain will cause the overshoot on the close speed loop to decrease, K_{aw} is chosen as $K_{aw} = 5 \cdot K_i$ in each control loop.
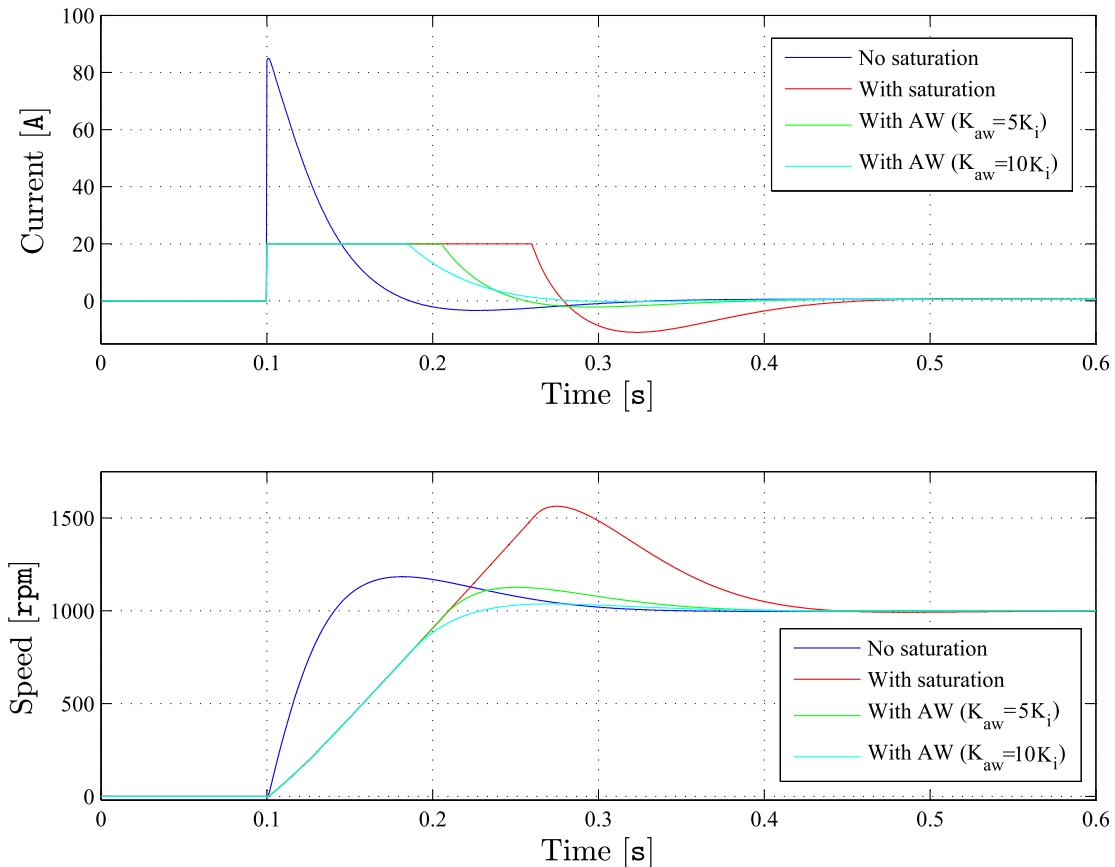
Figure 3.13. Current (top) and speed (bottom) response using anti windup [6].

As can be seen in the figure 3.13, where a step of 1000 RPM was performed, the response is better when $K_{aw} = 5 \cdot K_i$.

3.3.5 Voltage drops

Voltage drops can occur in the system due to:

1. Dead time in the inverter.

2. The internal connection in the inverter, the resistance of the cables and the on resistant transistors.

It is known that the time value for the death time is constant. When the inverter commands a small value of the current, the desire duty cycle for the voltage should be small, and the percentage of the dead time, in relation to the duty cycle time, is big. In the case that is studied in this report, medium and high speed, the drop voltage produced by the dead time is neglected because the current commanded is large enough.

The voltage drop of approximately 9 volts which appears in the dSPACE system [6] is accounted for in the simulation model by adding the voltage drop.

3.4 Simulation and Experimental results

In this section, the experimental results: current response and speed response, are presented. The simulations made with Simulink should result in the same behavior as those observed in the laboratory. The Control is implemented in the laboratory using dSPACE.

Table 3.1. Parameters used for simulation- and experimental verification.

System	Description	Parameter	Value	Unit
Current control	q-axis proportional gain	k_{qp}	2.5	[-]
	q-axis integral gain	k_{qi}	135	[-]
	d-axis proportional gain	k_{dp}	2.5	[-]
	d-axis integral gain	k_{di}	135	[-]
	Voltage limit	v_{lim}	85	[V]
Speed control	Proportional gain	$k_{\omega p}$	0.3	[-]
	Integral gain	$k_{\omega i}$	3.2	[-]
	Current limit	a_{lim}	20	[A]
Anti windup	Current integral gain	$k_{\omega aw}$	675	[-]
	Speed integral gain	k_{caw}	17.5	[-]

The table 3.1, shows the parameters obtained in the simulation which are implemented in the laboratory in order to compare the results.

3.4.1 Current loop

The rotor is locked at zero degrees in the laboratory to observe the current loop step response. The same is done in the simulations where the voltage drop is considered.
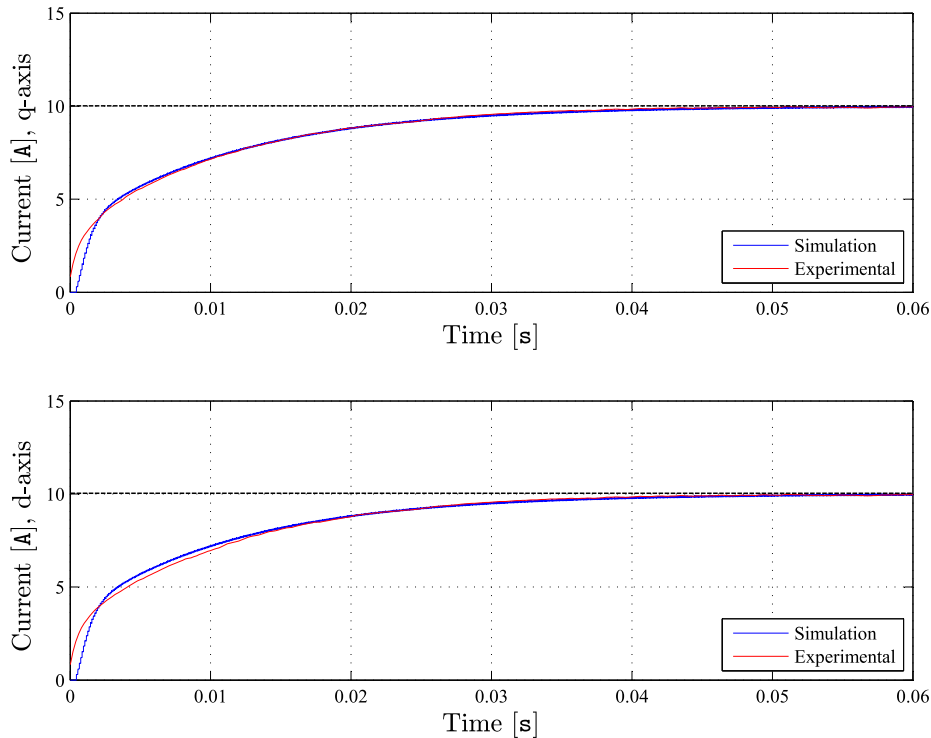

Figure 3.14. Experimental and simulated q-axis current loop step response (top) and d-axis current loop step response(bottom) after including in the model the dead time and internal inverter voltage drops.

Applying 10 amperes in the laboratory and in the simulation, the response is plotted in the same graph for the d-axis and q-axis and shown in Figure 3.14 where the voltage drop is considered.

The step response looks the same in the laboratory and in the simulations. The response characteristics can be considered similar enough to validate the simulation and to be considered acceptable.

3.4.2 Speed loop

In order to verify the speed loop response, it is tested at 1000 rpm speed step with zero load and at 10 Nm steep torque with 1000 rpm constant speed. The laboratory results are compared with the simulations. First, figure 3.15 present the speed step response.
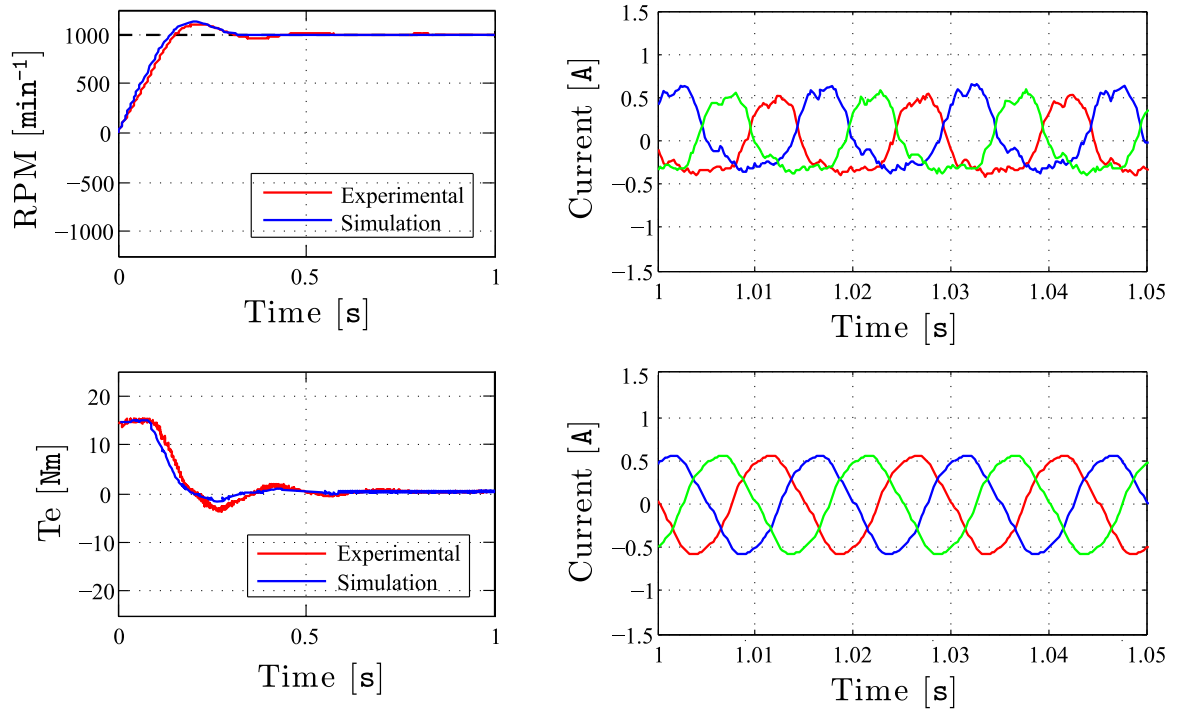

Figure 3.15. Experimental and simulated speed, torque, and current responses.

This is the most commonly used control system analysis where both the simulations and the laboratory, present similar characteristics for the rise time, the setting time and the overshoot. The torque and the currents respond accordingly, therefore J_0 and B_m are present in steady state in relatively the same scale.

Figure 3.16 below shows the next scenario. The system works perfectly with both -10 Nm and 10 Nm load torque. The values are very close in the simulations and the experimental results.
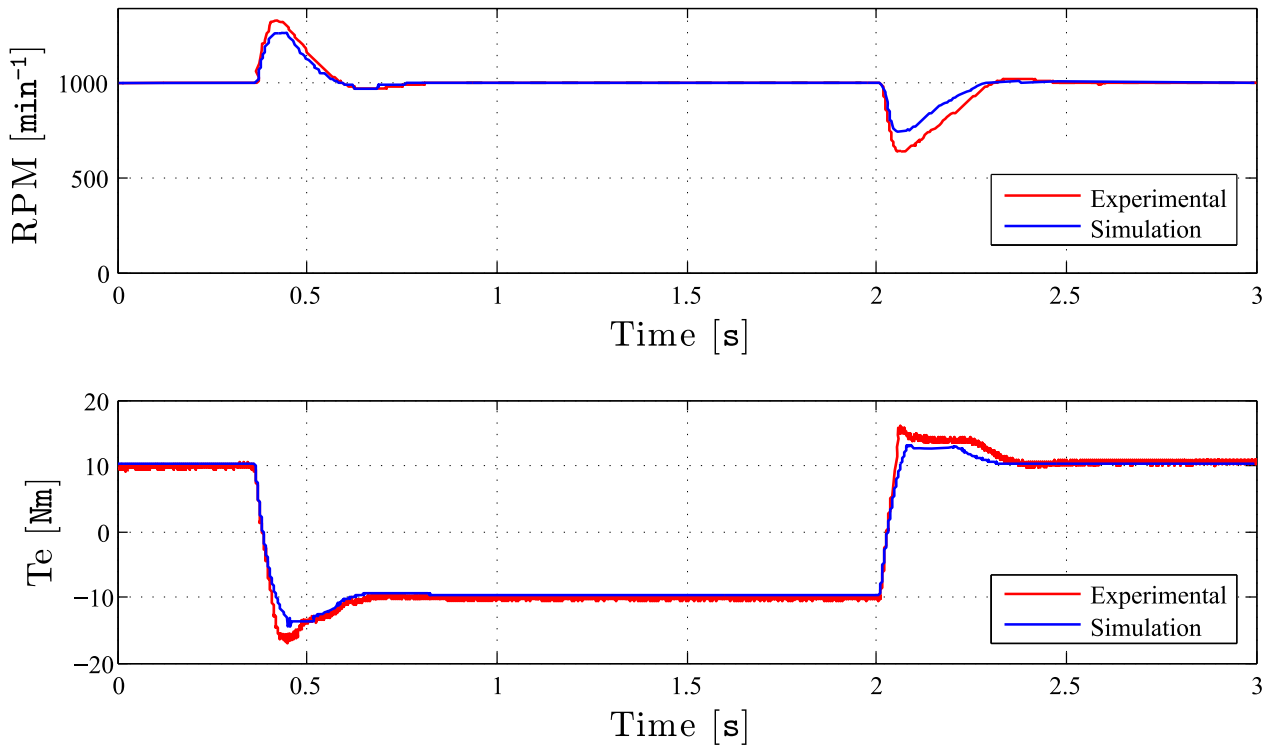
Figure 3.16. Experimental and simulated speed and torque response.

The divergences can be explained by several factors:

- Incorrect modeled moment of inertia.
- The coupling elasticity which is neglected in the simulations, but is present in reality.
- The simulation load torque is modeled as an ideal step, but in reality it is given by the IM.
- The static friction is neglected.

The moment of inertia is actually higher in the setup, therefore the rise time for the speed would slow down due to the anti windup system. The load is modeled as an ideal step/constant loads in the simulation, whereas the load torque in the setup comes from the IM that is not as precise as an ideal step/constant load.

Consequently, examining the different scenarios performed for both the actual dSPACE and the simulation speed loop, it can be concluded that the response for both are close enough to a satisfactory result.

Chapter 4

Sensorless Control

4.1 Introduction

The method FOC, presented in this project uses the speed and the position of the rotor to control the PMSM. This can be achieved easily using a sensor. The disadvantages in terms of reliability, machine size, noise interference and cost can be eliminated by removing the sensor and using a sensorless control.

A general sensorless classification for a PMSM is presented in this chapter where it can be divided in three strategies [12]:

- Model based estimators.

  - Nonadaptive Methods.
  - Adaptive Methods.
- Saliency Signal injection.
- Artificial Intelligence.

Model based estimators, Nonadaptive Methods: These methods use measured parameters of the PMSM as fundamental machine equations to estimate the position. They can be divided into four categories:

- Techniques using the measured DC-Link [16].
- Estimators using monitored stator voltages, or currents.
- Flux based position estimators.
- Position estimators based on back-EMF.

Model based estimators, Adaptive Methods: These are divided into four categories:

- Estimator based on Model Reference Adaptive System (MRAS).
- Observer-based estimators.
- Kalman estimator.
- Estimator which use the minimum error square.

Signal injection: After injecting voltage or current into the motor, the position and the speed can be determined by processing the results. This method is divided in two categories:

- High frequency: The injection signal is large enough to neglect the resistance of the motor, and the current depends only on the inductance.
- Low frequency: This method is based on the mechanical vibration of the rotor using low frequency (few Hz).

Artificial Intelligence

This describes neural network, fuzzy logic based systems and fuzzy neural networks [16].

This project is focused on an estimation of the speed and the position for medium and high speed using the Back-EMF based sensorless algorithm which is mature enough and has already been combined with vector control strategy in industrial applications. [20]. Therefore Back-EMF is selected to be implemented to estimate the position of the shaft. The stator flux linkage vector can be estimated to determine the rotor position angle using $\alpha\beta$ stationary reference frames, and then integrated into the equation, which can cause a drift. This problem can be avoided in different ways creating a sub-classification to the Back-EMF method. This is presented and studied in detail in the next section.

4.2 Position estimation

In this section, the method Back-EMF for a surface permanent magnet mounted position estimation, is introduced. This control algorithm is based on the estimation of the position using stator flux linkage space vector in stationary $\alpha\beta$-reference frames. The dynamics of the motor can be obtained by using the current and the voltage space vectors.
The mathematical structure of the estimation guarantees a high degree of robustness against parameter variation [4] and simplicity [19].
The voltage equations are represented in stationary $\alpha\beta$-reference frames assuming that the inductances are equal since the PMSM is surface mounted [19].

$$\begin{bmatrix} v_\alpha \\ v_\beta \end{bmatrix} = \begin{bmatrix} R_s & 0 \\ 0 & R_s \end{bmatrix} \cdot \begin{bmatrix} i_\alpha \\ i_\beta \end{bmatrix} + \frac{d}{dt} \begin{bmatrix} \lambda_\alpha \\ \lambda_\beta \end{bmatrix}$$

Where the stationary $\alpha\beta$ flux linkage can be expressed through the rotor position:

$$\begin{bmatrix} \lambda_\alpha \\ \lambda_\beta \end{bmatrix} = \begin{bmatrix} L_q & 0 \\ 0 & L_q \end{bmatrix} \cdot \begin{bmatrix} i_\alpha \\ i_\beta \end{bmatrix} + \begin{bmatrix} \cos\theta \\ sen\theta \end{bmatrix} \cdot \lambda_{pm}$$

So, from the above equations the position of the rotor can be estimated.

$$(4.1) \qquad \theta = \tan^{-1} \frac{\lambda_\beta - L_q \cdot i_\beta}{\lambda_\alpha - L_q \cdot i_\alpha} \qquad \texttt{[rad/s]}$$

The total flux linkage in stationary $\alpha\beta$-reference frames ($\lambda_{\alpha\beta}$) is now obtained by the equations 4.2 and 4.3:

$$(4.2) \qquad \lambda_\alpha = \int (v_\alpha - R_s \cdot i_\alpha) dt \qquad \texttt{[Wb]}$$

$$(4.3) \qquad \lambda_\beta = \int (v_\beta - R_s \cdot i_\beta) dt \qquad \texttt{[Wb]}$$

Where $\bar{i}_{\alpha\beta}$ is the current obtained from the LEM modules, $\overline{v}_{\alpha\beta}$ is obtained from the reference voltages given by the current controllers, R_s is the stator phase resistance, θ is the rotor angular position in

electrical radians, λ_{pm} is the peak value of the rotor PM flux linkage and L_q is the d-axis inductance. Formediumtohighspeedrange,changes to the resistancesand inductances because of thethermaleffects, can be neglected [10]

The problems that appear in this method, listed below, must be considered.

- Inaccurate measurements of inductance and resistance cause an error in the voltage that will cause a drift after the integration.
- A small drift in the current will cause increasing error after integration [10].

These problems can be eliminated by means of a compensating function [4]. In the following, the three different methods, Compensation block, Rasmussen and Rasmussen PI, will be introduced.

4.2.1 Compensation block

The voltage equation in stationary $\alpha\beta$-reference frames is show in the next equation 4.42:

$$\overline{v}_{\alpha\beta} = R_s \cdot \overline{i}_{\alpha\beta} + \frac{d\overline{\lambda}_{\alpha\beta}}{dt} \qquad [\mathtt{V}] \tag{4.4}$$

In this equation, the voltage, is calculated by measuring the current and the parameters of the machine, which are considered constants and accurate. Because this is not the reality, the margin of error can be compensated by introducing a voltage compensation v_{comp} and the equation then becomes:

$$\overline{v}_{\alpha\beta} = R_s \cdot \overline{i}_{\alpha\beta} + \frac{d\overline{\lambda}_{\alpha\beta}}{dt} - v_{comp} \qquad [\mathtt{V}] \tag{4.5}$$

v_{comp} compensates errors in the $\overline{\lambda}_{dq}$ estimation, such as inverter nonlinearity, dead time, integration offset and resistance variance [7].

v_{comp} is calculated to be a constant value where the flux linkage in stationary $\alpha\beta$-reference frames, calculated in different ways 4.7, 4.8, are compared and multiplied by a PI controlled 4.43, [10].

$$v_{comp} = \frac{K_{pcomp} \cdot s + K_{icomp}}{s} \cdot \left(\overline{\lambda}_{\alpha\beta} - \overline{\lambda}_{\alpha\beta}^{\widehat{\theta}} \right) \qquad [\mathtt{V}] \tag{4.6}$$

$$\overline{\lambda}_{\alpha\beta} = \int (v_{\alpha\beta} - R_s \cdot i_{\alpha\beta}) dt \qquad [\mathtt{Wb}] \tag{4.7}$$

$$\overline{\lambda}_{\alpha\beta}^{\widehat{\theta}} = \left(i_d^{\widehat{\theta}} \cdot L_d + \lambda_{pm} + j \cdot i_q^{\widehat{\theta}} \cdot L_q \right) \cdot e^{j\widehat{\theta}} \qquad [\mathtt{Wb}] \tag{4.8}$$

Where $\overline{\lambda}_{\alpha\beta}^{\widehat{\theta}}$ is the flux linkage in stationary $\alpha\beta$-reference frames obtained using the position estimated $\widehat{\theta}$ which can be calculated since the values of L_d, L_q, i_d, i_q, and λ_{pm} are known and K_{pcomp} and K_{icomp} are parameters that can be modified according to the needs of the system.

The drawback of the integral parameter in the PI controller is that the initial response is very slow, and the controller does not start to be effective until a certain amount of time has elapsed. Instead it cancels the remaining error, which could be present with a proportional controller.
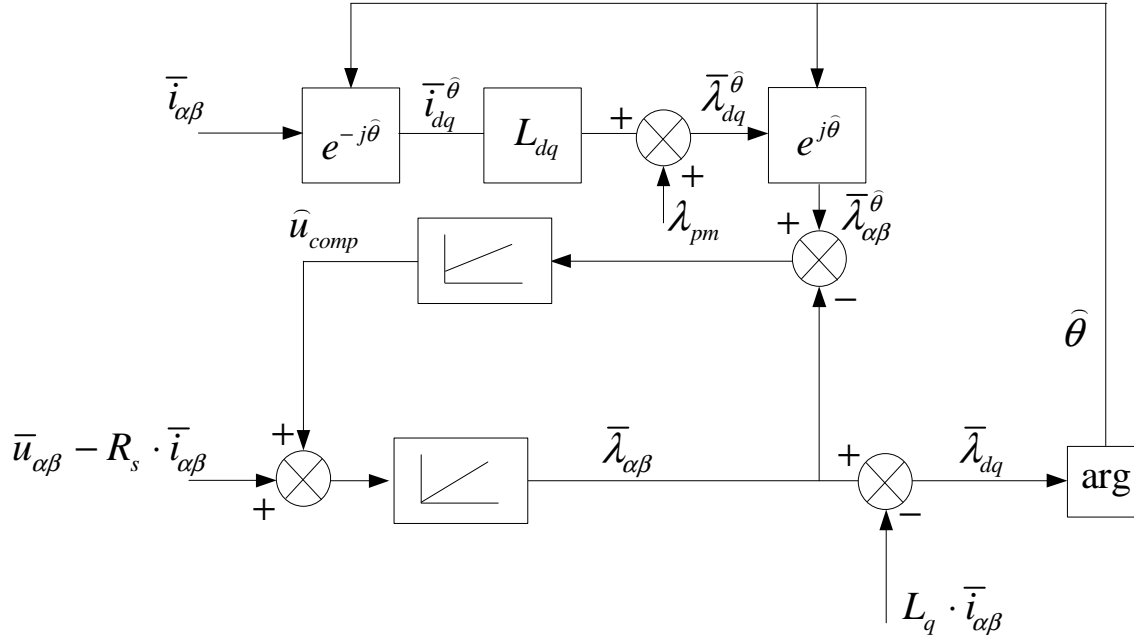

Figure 4.1. Diagram of the Back-EMF Compensation block method.

The diagram of the position estimation using the Compensation block method is show in figure 4.1.

4.2.2   Rasmussen

The Rasmussen Estimator method is presented in this section which estimates the rotor position using the parameters of the machine and eliminates the drift using dq-reference frame flux linkage. When $\overline{\lambda}_{dq}$ is estimated, to estimate the position, the voltage equation contains an offset produced because of the measurements. It is introduced and modeled as $\hat{u}_{off}$. Therefore a new equation 4.9 for the flux $\overline{\lambda}_{dq}$ become.

$$(4.9) \qquad \frac{\mathrm{d}\overline{\lambda}_{\alpha\beta}}{dt} = \overline{u}_s - R_s\overline{i}_s + \hat{u}_{off} \qquad \text{[V]}$$

$$(4.10) \qquad \overline{\lambda}_{dq} = \lambda_{pm} \cdot e^{j\hat{\theta}} \qquad \text{[Wb]}$$

$$(4.11) \qquad \overline{\lambda}_{\alpha\beta} = L_q \cdot i_{\alpha\beta} + \overline{\lambda}_{dq} \qquad \text{[Wb]}$$

Where $\hat{u}_{off}$ is designed to lead to the flux estimate with constant amplitude $\left|\overline{\lambda}_{dq}\right|$ [5].

$$(4.12) \qquad \hat{u}_{off} = C_1 \left(\lambda_{pm} - \left|\overline{\lambda}_{dq}\right|\right) e^{j\hat{\theta}} \qquad \text{[V]}$$

The figure 4.2 shows the structure of the estimation position reproduced through the mathematical equations using the Rasmussen method.
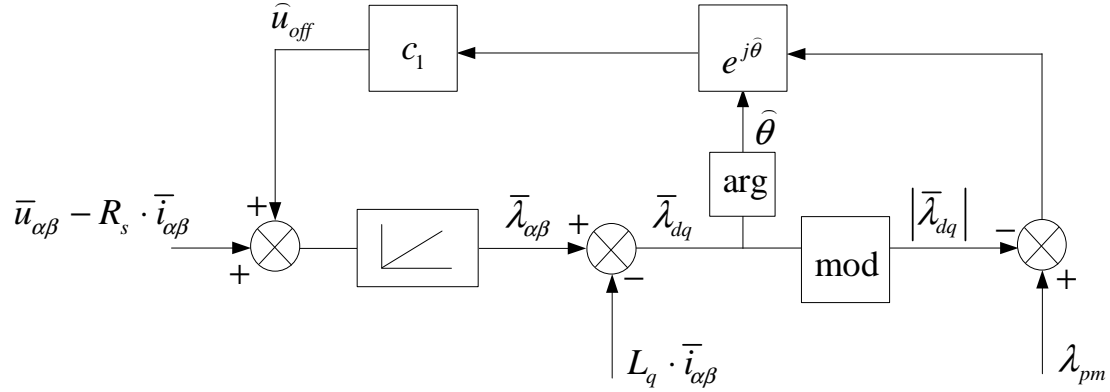

Figure 4.2. Diagram of the Back-EMF Rasmussen method.

The Rasmussen method is defined with a steady state error that depends on the parameters C_1, on the velocity measured in radians per second, and on δ_M defined in equation 4.13. δ_M turn depends on λ_{pm} and λ_M [5].

$$\delta_M = \frac{\lambda_{pm} - \lambda_M}{\lambda_M}$$ $\qquad$ [-] $\qquad$ (4.13)

$$\lambda_M = \left| \bar{\lambda}_{\alpha\beta} - L_q \cdot \bar{i}_{\alpha\beta} \right|$$ $\qquad$ [Wb] $\qquad$ (4.14)

$$\bar{\theta}_{ras} = -\frac{C_1}{\widehat{\omega}} \cdot \delta_M$$ $\qquad$ [rad] $\qquad$ (4.15)

This shall be taken into account when control is designed since the higher value of C_1 higher error and a low value will result in pure damping and low bias [5]. It can be observed in figure 4.14.

4.2.3 Rasmussen PI

A PI controller is introduced to the Rasmussen method. The constant C_1 is substituted in order to study the new response. So a new offset is defined in the next equation 4.16, called $\hat{u}_{offPI}$.

$$(4.16) \qquad u_{offPI} = \frac{K_{pras} \cdot s + K_{iras}}{s} \cdot \left(\lambda pm - \left| \overline{\lambda}_{\alpha\beta} \right| \right) \cdot e^{j\widehat{\theta}} \qquad [\text{V}]$$

Therefore the new structure for the Rasmussen PI method becomes:
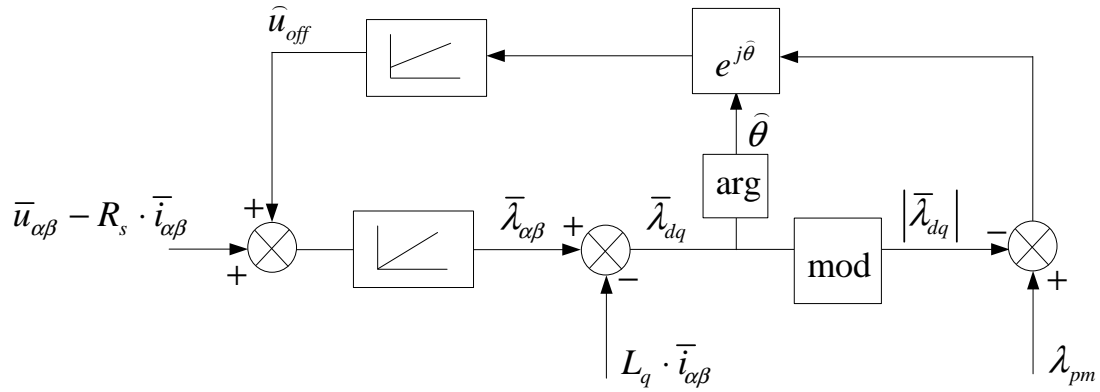
Figure 4.3. Diagram of the Back-EMF Rasmussen PI method.

4.2.4 Comparison methods

Figure 4.4 shows the flux linkage in stationary $\alpha\beta$-reference frames in order to demonstrate that the error produced by the drift has been removed. This is the main objective, and it is achieved for the three methods. The comparison is made using the following parameters for the different methods:

- Compensation method $K_{icomp} = 20$ $K_{pcomp} = 100$
- Rasmussen PI method $K_{iras} = 20$ $K_{pras} = 100$
- Rasmussen method $C_1 = 100$

These parameters are chosen looking for the most logical comparison while operating the PMSM at 1000 rpm speed with no load.
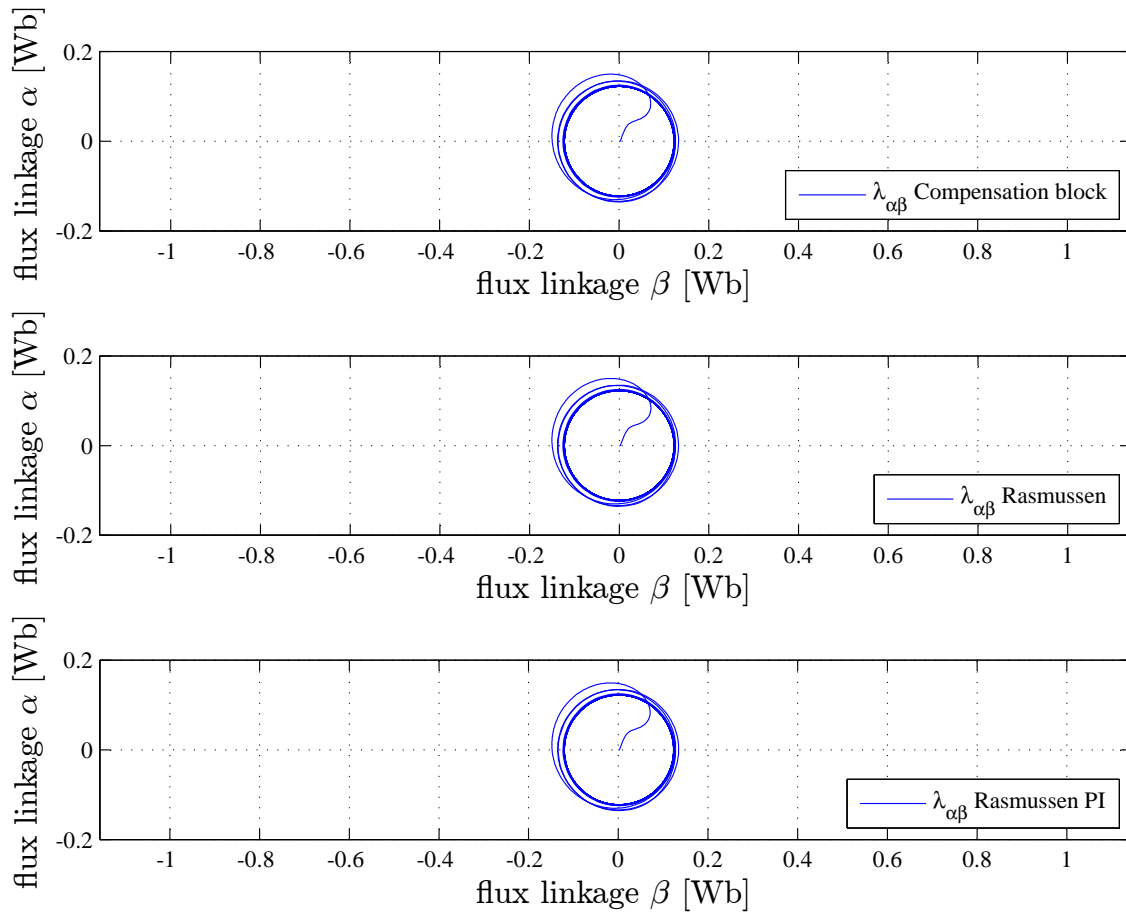
Figure 4.4. Simulation of the $\alpha\beta$ flux linkage obtain by the different methods

Between Rasmussen and Rasmussen PI method, the Rasmussen method with proportional control C_1 is the most appropriate choice for the control of the position estimation. Considering the permanent magnet flux linkage λ_{pm} as the input and the flux linkage in dq reference frames $\overline{\lambda}_{dq}$ as the output, the error is the difference between both. Considering this assumption, the close loop transfer function is considered to be a first order system. Therefore, it is clear that $\left|\overline{\lambda}_{dq}\right|$ and λ_{pm} should have the same value. Since it can be considered as a first order system, the disturbances are neglected. This first order system has a negative pole on the real axis which makes it stable, as can be seen in Figure 4.5.

By adding a PI controller, besides the proportional parameter, an integral parameter is also added.

Using the same assumption as before, where λ_{pm} is the input and $\overline{\lambda}_{dq}$ is the output, Rasmussen PI method results in a second order system for the close loop transfer function with two negative complex

conjugates poles on the real axis. This can make the response of the system critically stable, as seen in Figure4.5. Therefore the Rasmussen method is considered the best option.
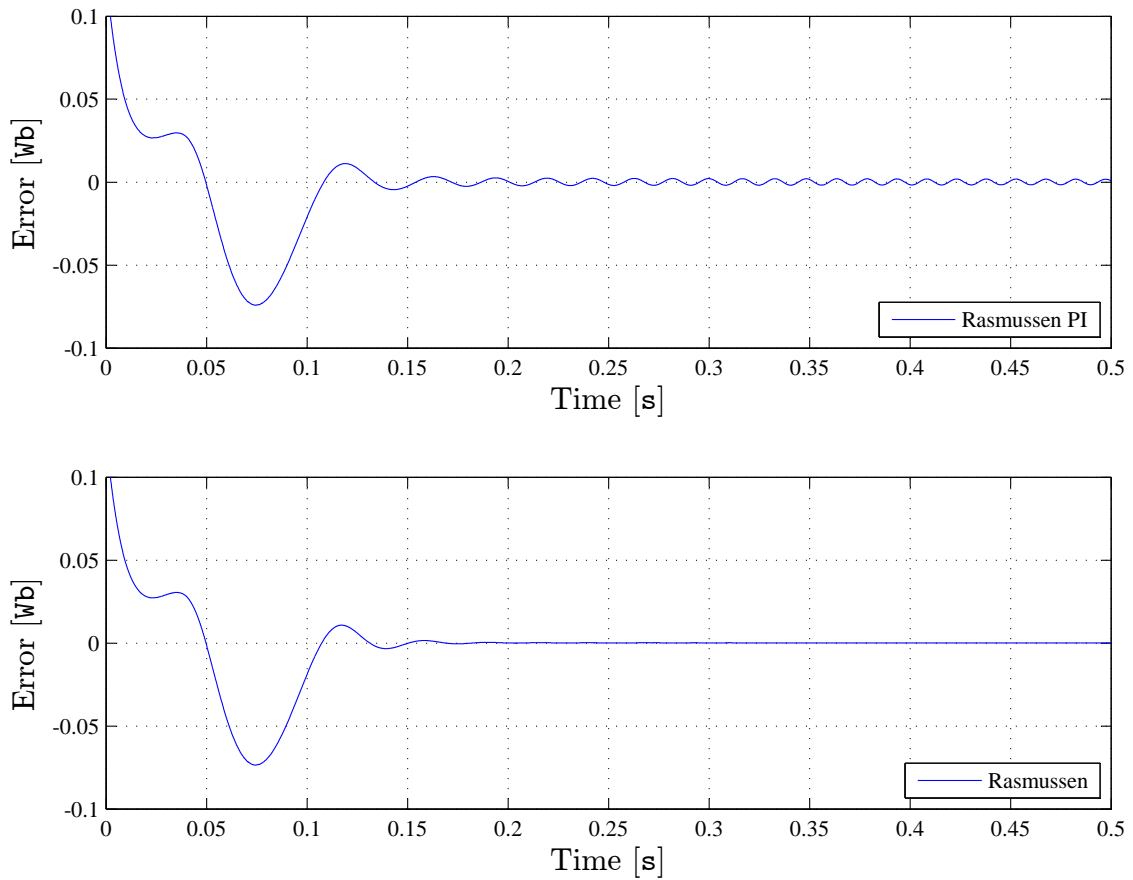

Figure 4.5. Simulation data of the difference between $|\lambda_{dq}|$ and the magnitude of λ_{pm}

Upon concluding that Rasmussen method is better than Rasmussen PI, the methods Compensation block and Rasmussen are compared.
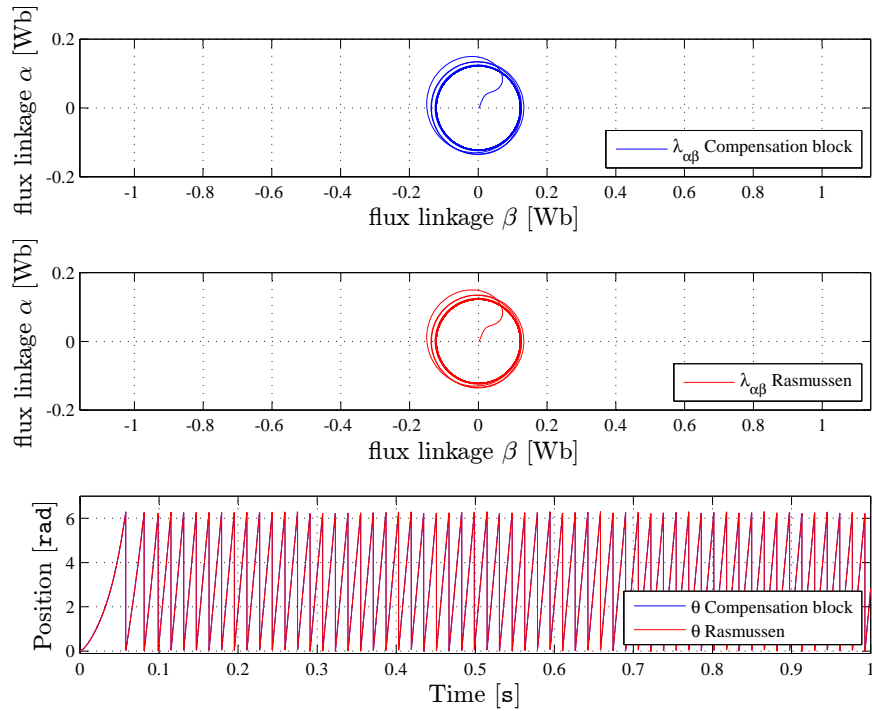
Figure 4.6. Simulation data of the $\alpha\beta$ flux linkage and the position estimated obtain by the Compensation block and Rasmussen methods.

Both Compensation block and Rasmussen method achieve good performances concluded with similar response characteristics in steady state and during the dynamics.

Rasmussen is the preferred method because of the simplicity in the control since there is only one parameter to control. Furthermore, Rasmussen method is the most recently developed method and therefore has not been researched extensively.

4.3 Inductance compensation

It is interesting to see from the equation 4.1, where the position is estimated, that L_d will not affect the rotor position. In medium to high speed range the uncertainties about the stator resistance variation due to thermal effect and inverter nonlinearities causing voltage estimation error can be safely neglected. Therefore it is considered L_q inductance as the only and most important parameter that will affect the estimated position error [11].

The inductance obtained from the machine is usually measured in an unsaturated region, and the parameters L_d and L_q are considered as constant values which are not reliable. The inductance value will decrease when the core of the machine is saturated, which occurs when the machine requires a high current.

Since L_q is considered constant, an error will appear when the current increases causing the inductance L_q to change.

When the core is saturated, no more magnetic flux can flow through the saturated section and therefore the flux can be determined as a constant value. The flux will increase when the current increases, but after saturation is reached, the change in the flux is negligible.

The flux linkage depends on B and S, where B is the magnetic field and S is the section of the material that the flux flows through. The section is a constant value and depends on the construction of the machine.

$$(4.17) \qquad\qquad \phi(B) = B \cdot S \qquad\qquad \text{[Wb]}$$

B(H) depends on the Magnetic Field Strength (H), and the inductance depends on the flux $\phi(H)$.

$$(4.18) \qquad\qquad L = \frac{N \cdot \phi}{i} \qquad\qquad \text{[H]}$$

In the saturated region, the flux does not change significantly, so increasing the current causes the inductance to decrease.

Introducing a flux linkage term $L_a \cdot \bar{i}_{\alpha\beta}$ in the stationary reference frame flux linkage the error can be analyzed [11]. Where L_a an arbitrary constant inductance.

$$(4.19) \qquad \bar{\lambda}_{\alpha\beta} = L_a \cdot \bar{i}_{\alpha\beta} + (L_a - L_q) \cdot \bar{i}_{\alpha\beta} + (\lambda_{pm} + (L_d - L_q) \cdot i_d) \cdot e^{j\theta} \qquad \text{[Wb]}$$

The term $\bar{i}_{\alpha\beta}$ is is replaced by $\bar{i}_{dq} \cdot e^{j\theta}$ and then the equation becomes

$$(4.20) \qquad\qquad \bar{\lambda}_{\alpha\beta} = L_a \cdot \bar{i}_{\alpha\beta} + \bar{\lambda}_{eq} \cdot e^{j\theta} \qquad\qquad \text{[Wb]}$$

where $\bar{\lambda}_{eq}$ represent a special flux linkage vector.

$$(4.21) \qquad \bar{\lambda}_{eq} = \lambda_{pm} + (L_d(i_d, i_q) - L_a) \cdot i_d + j \cdot (L_q(i_d, i_q) - L_a) \cdot i_q \qquad \text{[Wb]}$$

$$(4.22) \qquad \widehat{\theta} = \angle(\bar{\lambda}_{\alpha\beta} - L_a \cdot \bar{i}_{\alpha\beta}) = \angle\bar{\lambda}_{eq} + \theta \qquad [\text{rad}]$$

The position error due to inductance variation is show in the equation 4.23.

$$(4.23) \qquad \bar{\theta}_{err} = \angle\bar{\lambda}_{eq} = \tan^{-1} \frac{(L_q(i_d, i_q) - L_a) \cdot i_q}{\lambda_{pm} + (L_d(i_d, i_q) - L_a) \cdot i_d} \qquad [\text{rad}]$$

Figure 4.7 shows the position error, according to the equation 4.23, the real and the estimated rotor position.
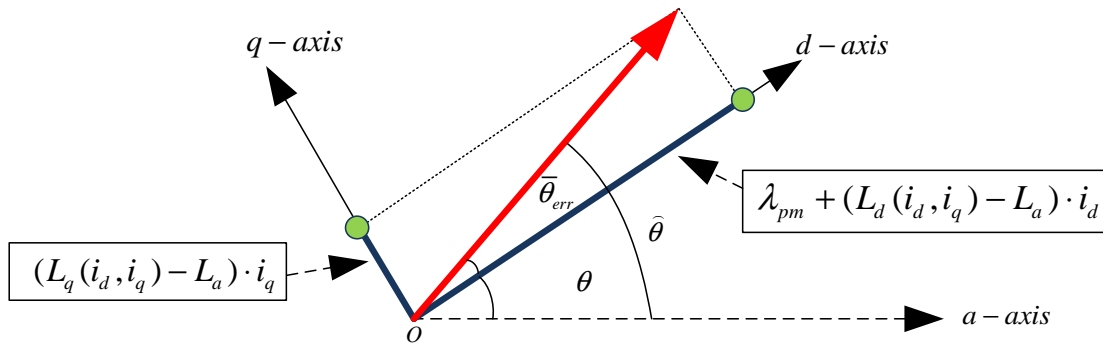
Figure 4.7. Vector position error produced by the inductance variation [11].

As seen from Figure 4.8, when L_a is considered as the unsaturated inductance value, an error will appear when the current increases, causing the inductance L_q to change because the machine is in the saturated region.
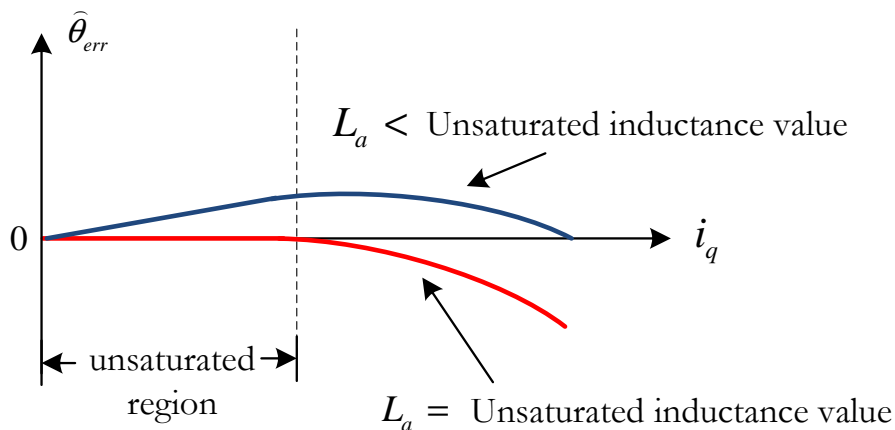

Figure 4.8. Position error produced by artificial L_a [11].

The error can be reduced by 50%, by calculating the appropriate $L_a <$ unsaturated inductance value, using equation 4.23.

4.3.1 Experimental study of the position error

In this section the rotor position error is measured by applying torque in order to experimentally validate and verify the theory. At steady state the motor is running at 500 rpm and a load change is introduced by the IM. It can be observed from the Figures 4.9, 4.10,4.11 that increasing the load will cause the error to incrementally increase.
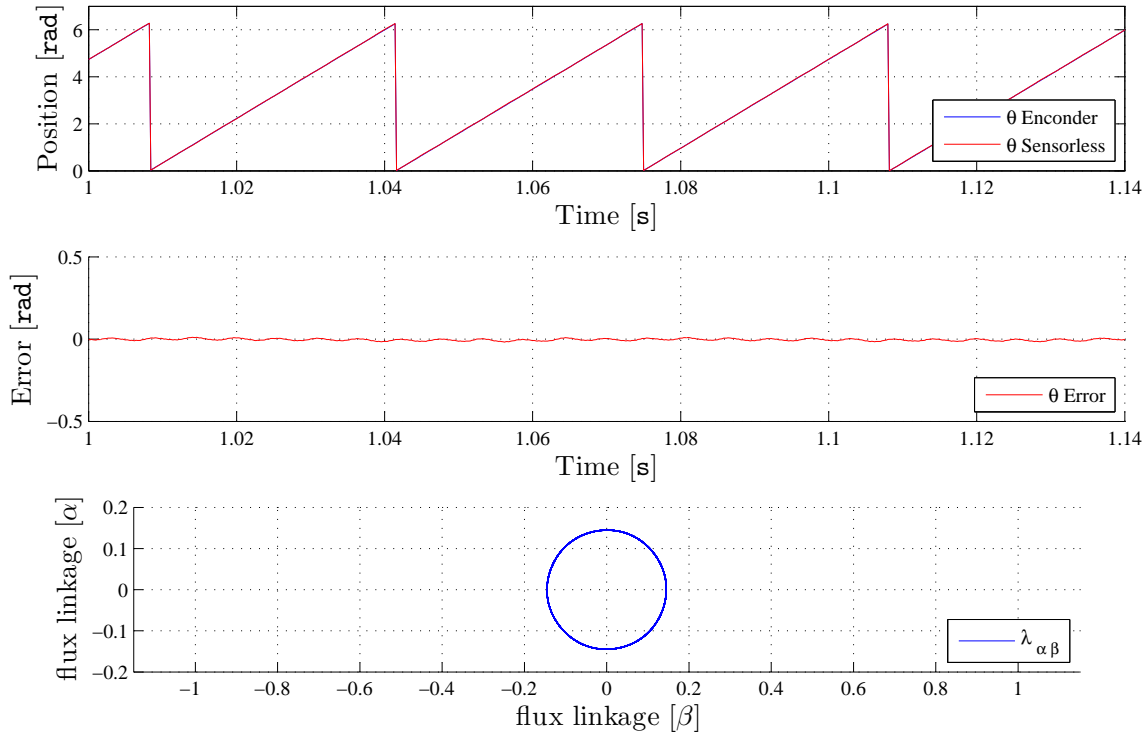

Figure 4.9. Laboratory position error and $\alpha\beta$ flux linkage, at 5.5 Nm load condition ($i_q = 7.5$ A).

The error produced in the Figure 4.9 does not increase excessively. This can be explained due to the fact that the core does not reach the saturation region when the load is Torque = 5.5 Nm and the current $i_q = 7.5$ A.

In contrast, the Figures 4.10 and 4.11 show an increased error, indicating that the iron core is in the saturation region.

Knowing the unsaturated inductance value $L_a = 0.0022$ H and the position error $\bar{\theta}_{err} = -0.075$ rad when the current is at the maximum $i_q = 26.5$ A, the new value of $L_q(i_d, i_q)$ is calculated. The error is reduced by 50% just by applying the above equation 4.23. The new value of the inductance is $L_{anew} = 0.002$ H. Considering $L_{anew} = L_q$, this is applied in equation 4.1 of the estimated position.

$$\bar{\theta}_{err} = \tan^{-1} \frac{(L_q(i_d, i_q) - L_a) \cdot i_q}{\lambda_{pm} + (L_d(i_d, i_q) - L_a) \cdot i_d} \qquad \text{[rad]} \tag{4.24}$$

$$L_q(i_d, i_q) = 0.00185 \qquad \text{[H]} \tag{4.25}$$

$$L_{anew} = \frac{L_a - L_q(i_d, i_q)}{2} + L_q(i_d, i_q) \approx 0.002 \qquad \text{[H]} \tag{4.26}$$
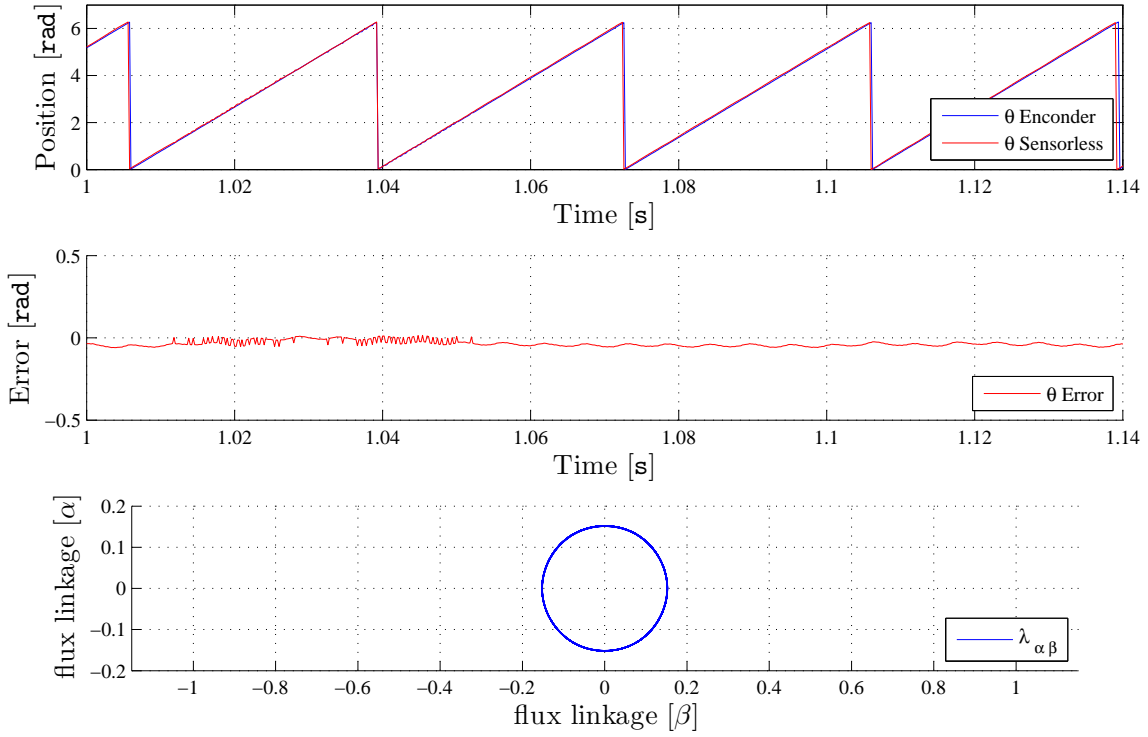
Figure *4.10.* Laboratory position error and $\alpha\beta$ flux linkage, at 12 Nm load condition ($i_q = 16.3$).
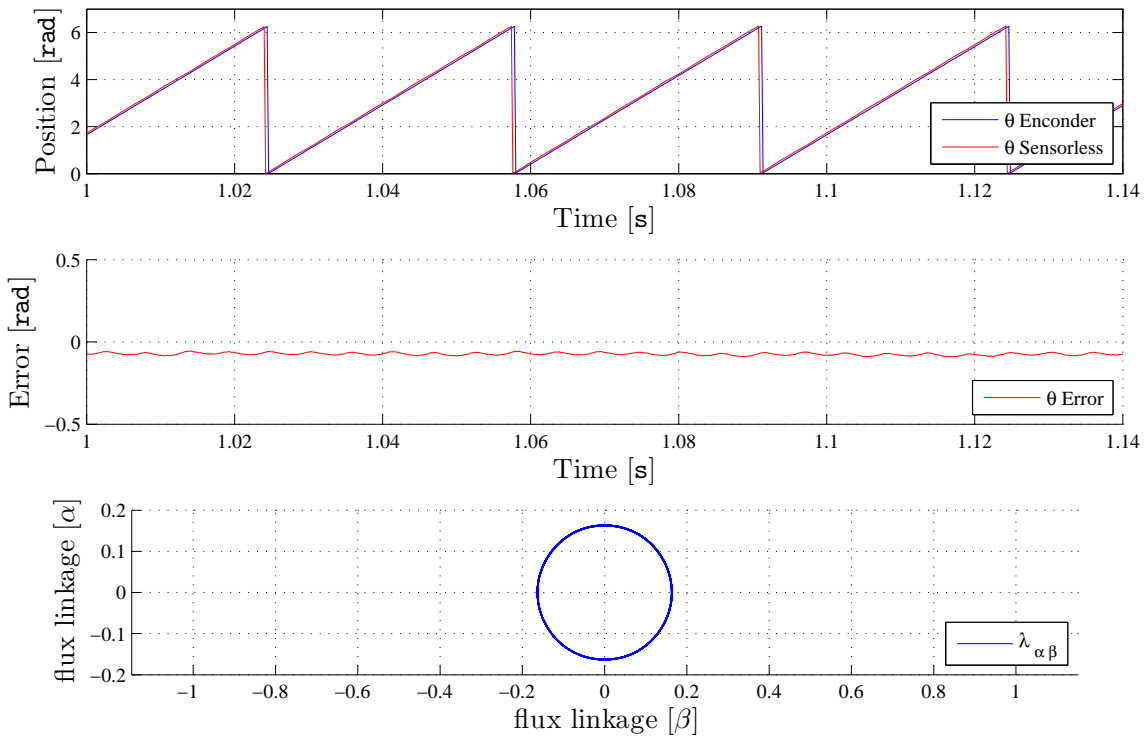

Figure *4.11.* Laboratory position error and $\alpha\beta$ flux linkage, at 19.5 Nm load condition ($i_q = 26.7$).

Therefore the theory is verified experimentally, where the error is explained by the equations 4.23

4.4   Speed estimator

In this report a Phase-Locked Loop (PLL) is designed to obtain the estimated speed. The block diagram of the PLL is shown in Figure 4.12. It introduces a PI controller in the open loop that contains two important parameters K_{ep} and K_{ei}. The integral of the speed is the position. Therefore after the integral in the closed loop the position can be retrieved.
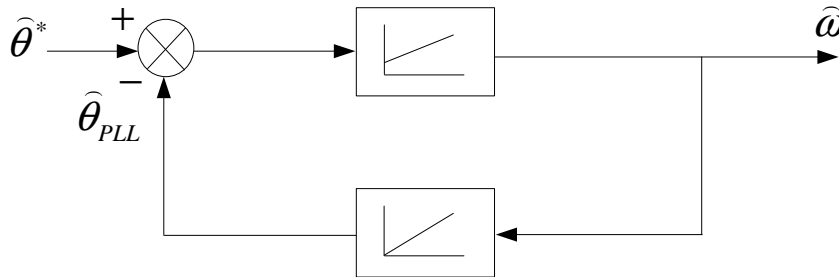

Figure 4.12. Phase lock loop (PLL) diagram.

Based on Figure 4.12 above, a new value of the position estimation θ^{PLL} is obtained.

$$(4.27) \qquad \theta^{PLL} = \frac{1 \cdot K_{ep} \cdot S + K_{ip}}{s^2} \cdot \left(\theta - \theta^{PLL}\right) \qquad [\texttt{rad}]$$

The transfer function in the Laplace domain is obtained in order to design the parameters K_{ep} and K_{ei}, where θ_r^{PLL} is the output and θ_r the input.

$$(4.28) \qquad \frac{\theta^{PLL}}{\theta} = \frac{K_{ep} \cdot s + K_{ip}}{s^2 + K_{ep} \cdot s + K_{ip}} \qquad [\text{-}]$$

Where θ_r^{PLL} is equal to θ_r in steady state. Therefore the error is zero.

4.5 Control design

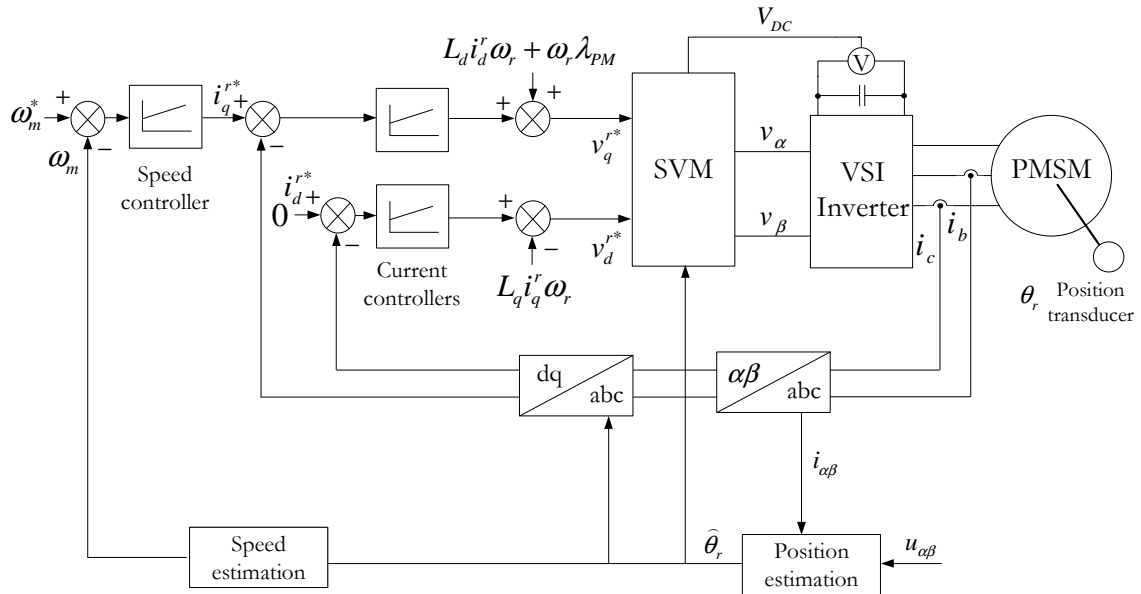The control structure for sensorless control is shown in Figure 4.13.

Figure 4.13. General sensorless scheme using Field Oriented Control.

The position estimation takes the values of the current and voltage in stationary $\alpha\beta$-reference frames for the back-EMF Rasmussen method and the speed estimation takes the position for the PLL.

4.5.1 Position estimator

The Back-EMF Rasmussen based position estimation algorithm has a constant parameter that can be controlled. The parameter is called C_1 which is multiplied by the difference between $|\lambda_{dq}|$ and λ_{pm}. It is introduced in equation 4.16 where the offset is altered to eliminate the drift. C_1 the response will be faster in the dynamics "The higher C_1 the higher speeds that could be reached and vice versa for lower speeds"[13]. This make sense because, as it is mentioned in [5] "C_1 is a balance between damping and bias, meaning that a low value will result in pure damping and low bias and visa versa".

$|\lambda_{dq}|$ response, which depends on C_1, is also investigated. This response is faster with a higher value of C1 and vice versa. The time response also depends on the error between $\left|\overline{\lambda}_{dq}\right|$ and λ_{pm}, being faster the higher the error, so it is continuously adapted to demand.

C_1 is determined in terms of $\left|\overline{\lambda}_{dq}\right|$, speed and position response running the machine from the worst-case scenario which is the lower speed when C_1=50 and the speed is 200 rpm.
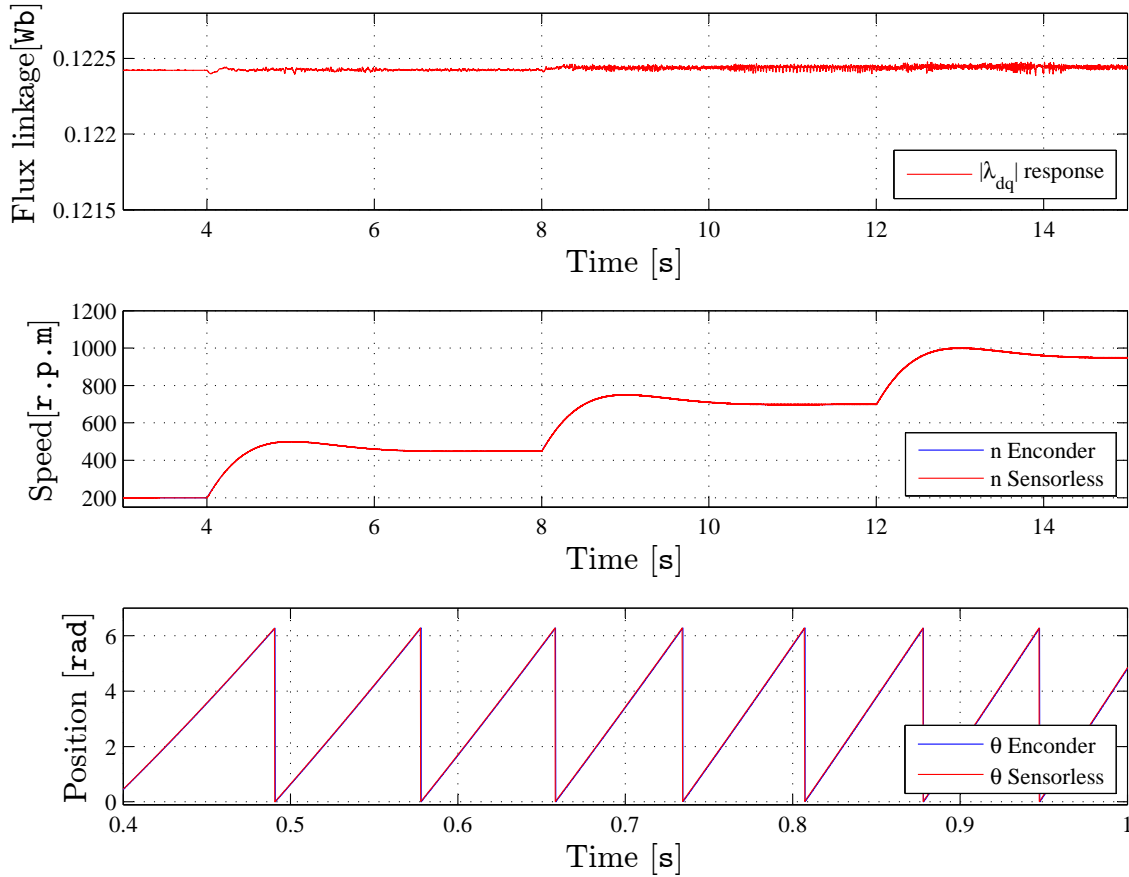
Figure 4.14. Response of the $\left|\overline{\lambda}_{dq}\right|$, Speed and the position estimated. When $C_1 = 50$ and the speed PI controllers are $K_i w$=0.1 and $K_w p$=0.05

From Figure 4.14 it can be seen that for higher speeds, with the same value of C_1, difference between λ_{pm} and λ_{dq} decreases knowing $\lambda_{dq} = 0.12258$ Wb. Additionally the figure shows that the response is fast enough with values of $C_1 = 50$.

Thus, according to the equations 4.13 and 4.15, the ratio C_1 divided by $\widehat{\omega}$ is set as a constant value so C_1 will be capable of different speeds values.

Being able to increase the C_1 value in the equation 4.15 for higher speeds, improves the response and maintains a constant error value. The ratio is assigned to be $C_1 / \widehat{\omega} = 0.6$.

4.5.2 Speed estimator

In this section, the parameters of the PLL are tuned in order to get the required response.

The PLL transfer function can be rewritten as a standard second order transfer function 4.29.

$$(4.29) \qquad \frac{\theta_r^{PLL}}{\theta_r} = \frac{K_{ep} \cdot S + K_{ip}}{S^2 + K_{ep} \cdot S + K_{ip}} = \frac{\omega_n^2}{S^2 + 2 \cdot \xi \cdot \omega_n + \omega_n^2} \qquad [\text{-}]$$

The existing relation between both transfer functions allows the PI_PLL controllers parameters, K_{ei} and K_{ep}, to be calculated when [2] the desired bandwidth and damping ratio are known.

$$(4.30) \qquad K_{ep} = B_\omega \left(2.2 \cdot \xi - 0.668 \cdot \xi^2\right) \qquad [\text{-}]$$

$$(4.31) \qquad K_{ei} = B_\omega^2 \left(1.1 - 0.334 \cdot \xi\right)^2 \qquad [\text{-}]$$

From the relation in the equation 4.32, ω_r can be calculated which is the input frequency of the PLL

$$(4.32) \qquad \omega = \frac{n \cdot 2 \cdot \pi \cdot pp}{60} \qquad [\texttt{rad/s}]$$

Where the bandwidth can be related to the input frequency, as is shown in the following equation, fulfilling the condition 4.33.

$$(4.33) \qquad 0 \leqslant \omega \leqslant Bw \qquad [\texttt{rad/s}]$$

So the equation 4.34 is assumed in order to tune the PI_{PLL} parameters.

$$(4.34) \qquad \omega = Bw \qquad [\texttt{rad/s}]$$

Therefore from Bw the control parameters can been calculated:

$$(4.35) \qquad K_{ep} = Bw \left(2.2 \cdot \xi - 0.668 \cdot \xi^2\right) \qquad [\text{-}]$$

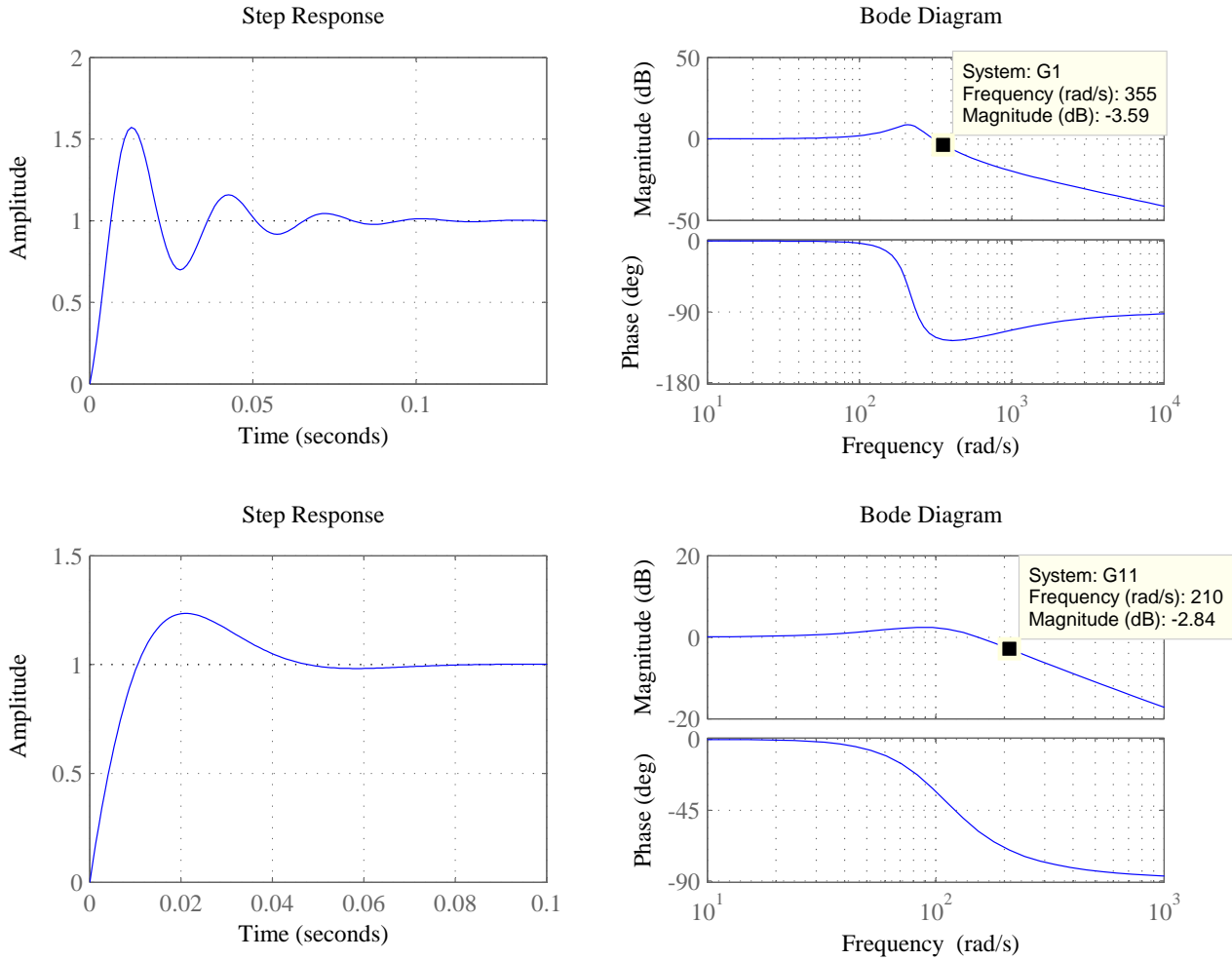$$(4.36) \qquad K_{ei} = Bw^2 \left(1.1 - 0.334 \cdot \xi\right)^2 \qquad [\text{-}]$$

Figure *4.15*. Speed close loop unit step response and close loop bode diagram with old PI controllers (top graphs) and new PI controllers (bottom graphs) showing the bandwidth

For different speed values, the corresponding frequency determines the bandwidth and consequently the final values for K_{ep} and K_{ei} where the damping ratio is set as $\xi = 0.2$. In the case studied when n=500 rpm, the condition 4.33 is fulfilled, where $\omega = 209.43$ rad/s.

$$(4.37) \qquad \omega = \frac{n \cdot 2 \cdot \pi \cdot pp}{60} = \frac{500 \cdot 2 \cdot \pi \cdot 4}{60} = 209.43 \qquad [\texttt{rad/s}]$$

Figure 4.15 shows the bandwidth when applying the above assumption to the equations 4.35 and 4.36 where the value is too large (Bw=355 rad/s). It can be a problem when higher frequencies than ω_r appear in the rotor position.

In order to eliminate the undesired frequencies, we use the frequency in Hz so ω_r will decrease $2 \cdot \pi$ and then, the bandwidth becomes smaller. The equations 4.45 and 4.39 [17] are used increasing K_{ep} ten times. Bw = 215 rad/s is the new and more appropriate bandwidth for fulfilling the condition 4.33.

$$(4.38) \qquad PI_{PLL} = K_{ep}\left(1 + \frac{1}{T_i \cdot s}\right) \qquad [\text{-}]$$

$$(4.39) \qquad\qquad K_{ep} = \frac{9.2}{t_s} \qquad\qquad [\text{-}]$$

4.5.3 Sensorless

When the system operates without an encoder, the speed loop parameters should be modified. A delay is introduced, as a feedback in the system, by the position and speed estimation as it is shown in Figure 4.16. In this way, the variation of the poles can make the system unstable.
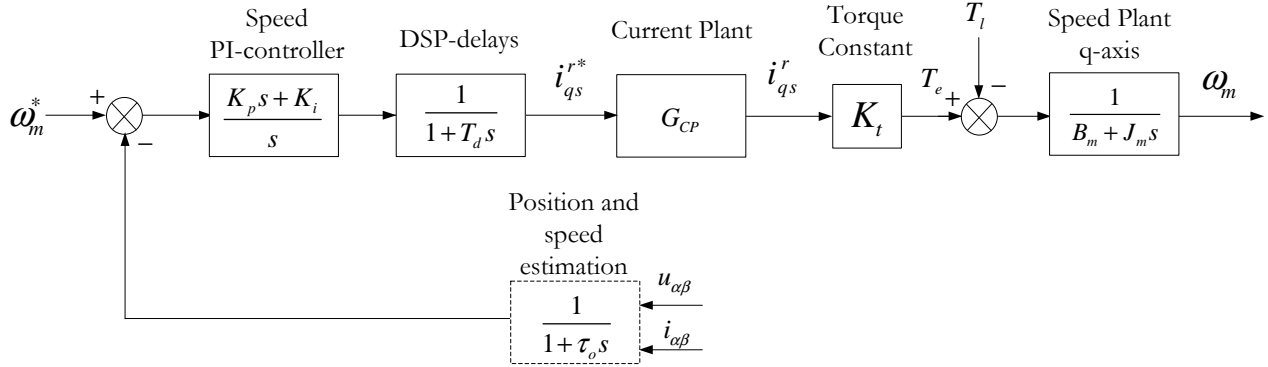

Figure 4.16. speed close loop where the sensorless control is used as the feedback.

Where τ_0 is defined as a time constant. The new close loop transfer function becomes:

$$(4.40) \qquad\qquad G_{cl}(s) = \frac{G(s)}{1 + G(s) \cdot H(s)} \qquad\qquad [\text{-}]$$

where:

$$(4.41) \qquad\qquad H(s) = \frac{1}{1 + \tau_0} \qquad\qquad [\text{-}]$$

The higher value of τ_0 is used for the control because it causes the worst case. By applying this assumption, the bandwidth is calculated when the system is running at 200 rpm which can be obtained from the bode plot. By applying a simplification, the second order closed loop PLL transfer function is considered as a first order system.

$$(4.42) \qquad\qquad H(s) = \frac{1}{1 + \tau_0} \qquad\qquad [\text{-}]$$

where τ_0 is determined based on the sensorless bandwidth using the equation 4.43.

$$(4.43) \qquad\qquad Bw = \frac{1}{\tau_0} \qquad\qquad [\texttt{rad/s}]$$

The figure 4.17 below shows the bode diagram in close and open loop, and the root locus, using the new control values K_i and K_p for the PI speed loop controller where PI controllers are adjusted until a phase margin of 40° - 60° is reached (no disturbance)[14].
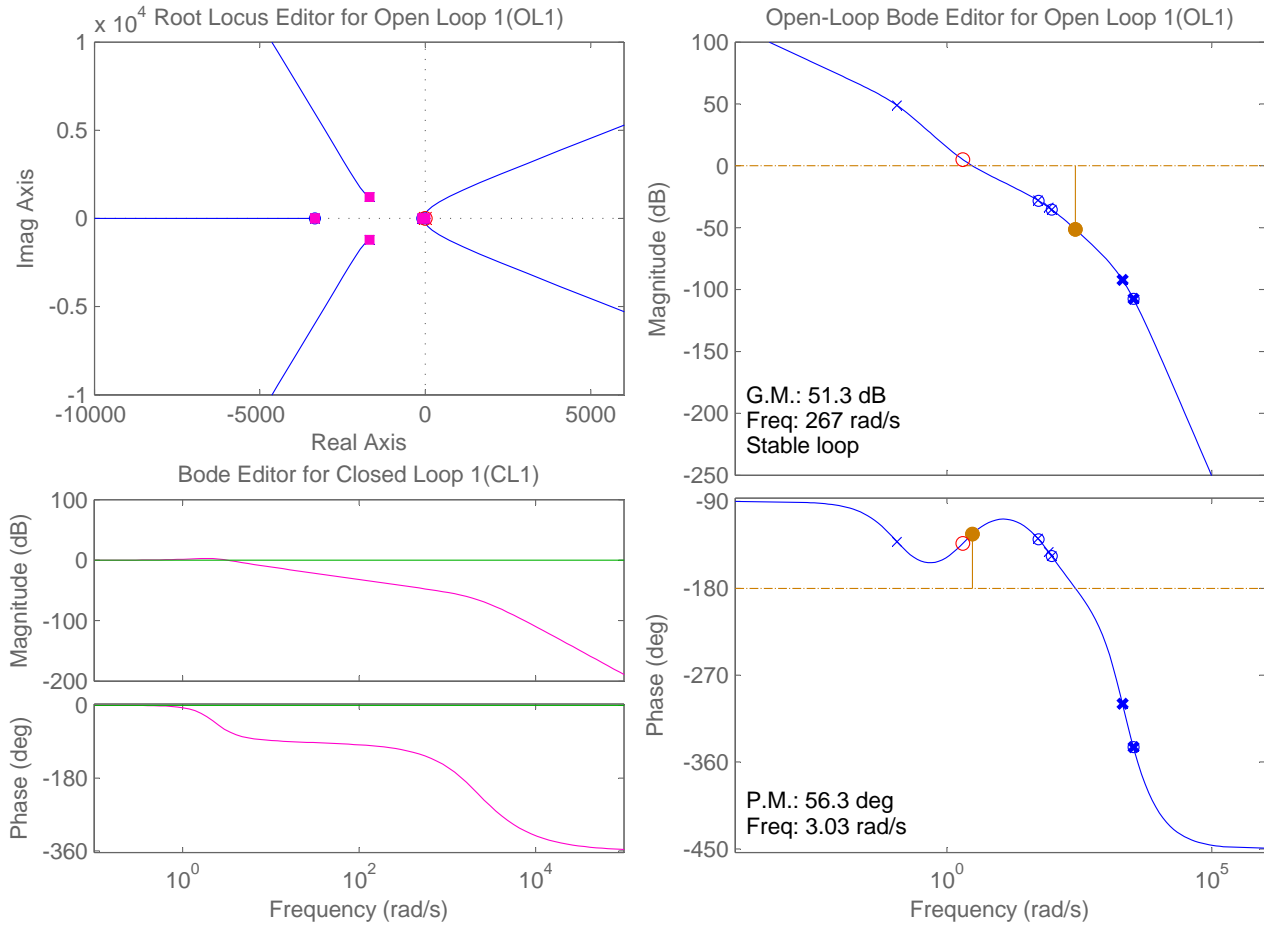
Figure 4.17. Open and close loop Bode diagram and root locus for speed controller.

The control values for the estimation of speed and position are selected as shown in Table 4.1. Once the correct estimate has been made for speed and position the FOC is updated. The parameters shown will be implemented for both the simulation and in the laboratory.

Table 4.1. Parameters used for sensorless control.

System	Description	Parameter	Value	Unit
Current control	q-axis proportional gain	k_{qp}	2.5	[-]
	q-axis integral gain	k_{qi}	135	[-]
	d-axis proportional gain	k_{dp}	2.5	[-]
	d-axis integral gain	k_{di}	135	[-]
	Voltage limit	v_{lim}	85	[V]
Speed control	Proportional gain	$k_{\omega p}$	0.05	[-]
	Integral gain	$k_{\omega i}$	0.1	[-]
	Current limit	a_{lim}	20	[A]
Anti windup	Current integral gain	$k_{\omega aw}$	675	[-]
	Speed integral gain	k_{caw}	17.5	[-]

4.5.4 Auto tuning

Based on the control design, the parameters of the PI_{PLL} and the Back-EMF Rasmussen method control can be modified in relation to the speed operation in order to get a better response.

Figure 4.18 shows the new schematic version of the control where the Auto-tunings are implemented on the position and speed estimation based on the reference speed.
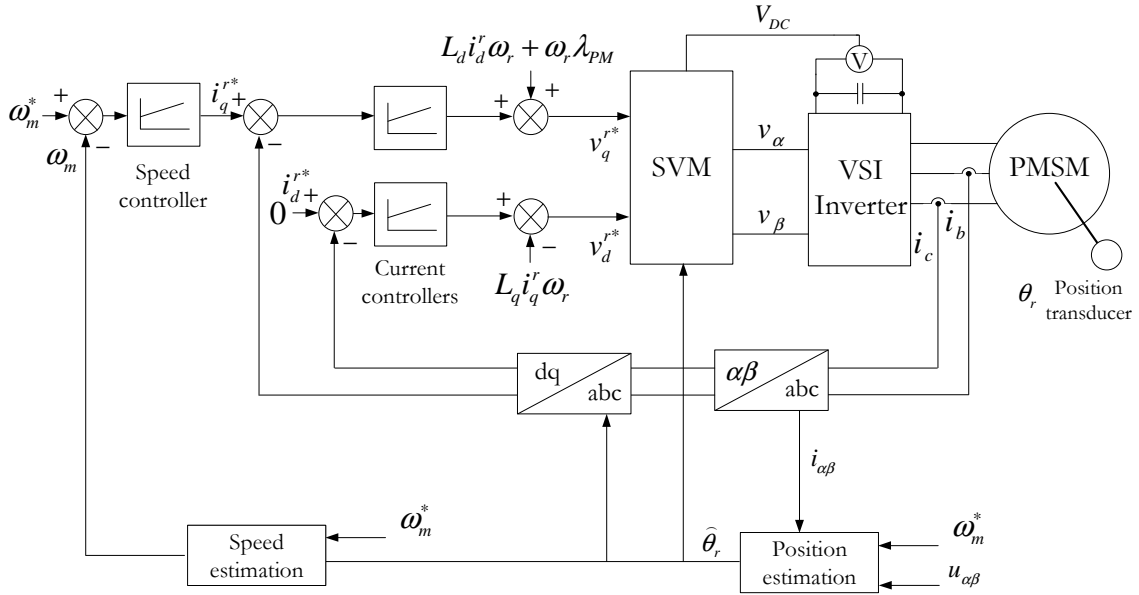

Figure 4.18. General sensorless auto-tuning scheme using Field Oriented Control.

when the reference speed is known, the frequency of the input variables in the sensorlees control are also known, and therefore the PI controller should be changed in order to adapt the Bandwidth.

The block diagram 4.19 of the position estimation control system of PMSM by auto-tuning C_1 shown how it is implemented.
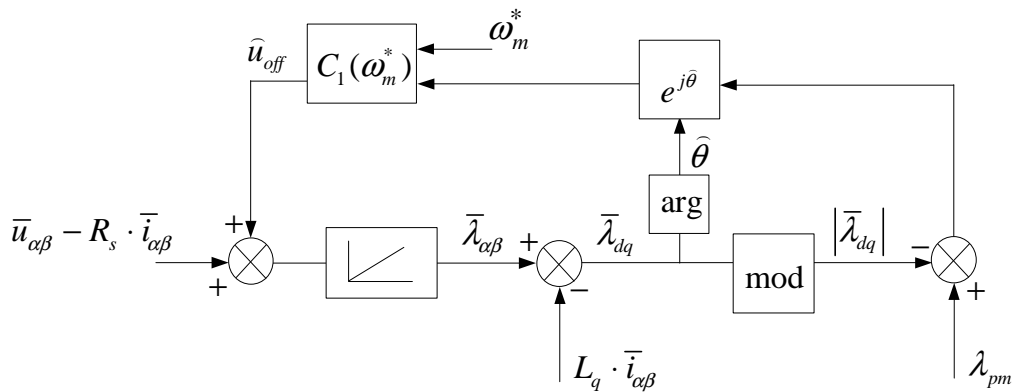

Figure 4.19. Diagram of the position estimation with auto-tuning.

The concept of the Rasmussen control includes auto-tuning making the response faster when the difference between $\left|\overline{\lambda}_{dq}\right|$ and λ_{pm} increases and vice versa. The parameter C_1 makes it even faster. Therefore tuning C_1 to the worst case, based on the control of the equation 4.15, the ratio $C_1/\overline{\omega}$ is kept constant. This allows C_1 to be increased for higher speeds without increasing the error. The equation 4.46 shows the C_1 Auto-tuning control where $\widehat{\omega}$ is considered to be the same as the reference estimated ω^* and the ratio $C_1/\overline{\omega} = 0.6$.

The block diagram 4.20 of the speed estimation control system of PMSM by auto tuning the PI_{PLL} parameters shows how it is implemented.

Figure 4.20. Diagram of the speed estimation with auto-tuning .

Based on the control design, the parameters of the PI_{PLL} must be auto tuned in relation to the speed reference using the equations 4.44 and 4.45

$$K_{ep}(\omega^*) = \left(\frac{\omega^*}{2 \cdot \pi} \cdot \left(2.2 \cdot \xi - 0.668 \cdot \xi^2 \right) \right) \cdot 10 \qquad [\text{-}]$$
(4.44)

$$K_{ei}(\omega^*) = \left(\left(\frac{\omega^*}{2 \cdot \pi} \right)^2 \cdot (1.1 - 0.334 \cdot \xi)^2 \right) \cdot 10 \qquad [\text{-}]$$
(4.45)

When the Auto-tuning is done, a problem appears if the machine has a reference speed of zero. At zero speed, C_1 is equal to zero, meaning that the Rasmussen method is not working, and therefore, the drift will appear after the integral. This is solved by adding a constant value K_1 as is shown in the equation 4.46. The value K_1 is assigned as $K_1 = 10$.

$$C_1(\omega^*) = 0.6 \cdot \omega^* + K_1 \qquad [\text{-}]$$
(4.46)

As an example the values of the PI_{PLL} controller and C_1 are calculated using the Auto-tuning when the reference speed $n^* = 500$ rpm. The value of $\omega^* = 209.43$ rad/s is calculated using following equation 4.47.

$$\omega^* = \frac{n^* \cdot 2 \cdot \pi \cdot p_p}{60} \qquad [\text{rad/s}]$$
(4.47)

Knowing the reference speed $\omega^* = 209$ rad/s, the damping ratio $\xi = 0.2$ and the constant $K_1 = 10$, the parameters of the controllers can be calculated using equations 4.46, 4.45 and 4.44: $C_1(\omega^*) = 310$, $K_{ep}(\omega^*) = 137.8$ and $K_{ei}(\omega^*) = 1861$.

Chapter 5

Sensorless Experimental results

In this chapter the laboratory results for the sensorless rotor field oriented control of PMSM are presented by several setup scenarios. The position and the speed are measured by the encoder in order to compare and verify the results obtained the by sensorless control algorithm, using the Auto-tuning for both the position estimation and the speed estimation.

In each of the graphs below showing position error, errors above 0.5 are as a result of errors in the measurements.

5.1   Speed steps with no load.

In this case, the sensorless control is tested with no load for both negative and positive speed values which are applied incrementally in speed steps.

5.1.1   Decreasing and increasing steps at positive speed.
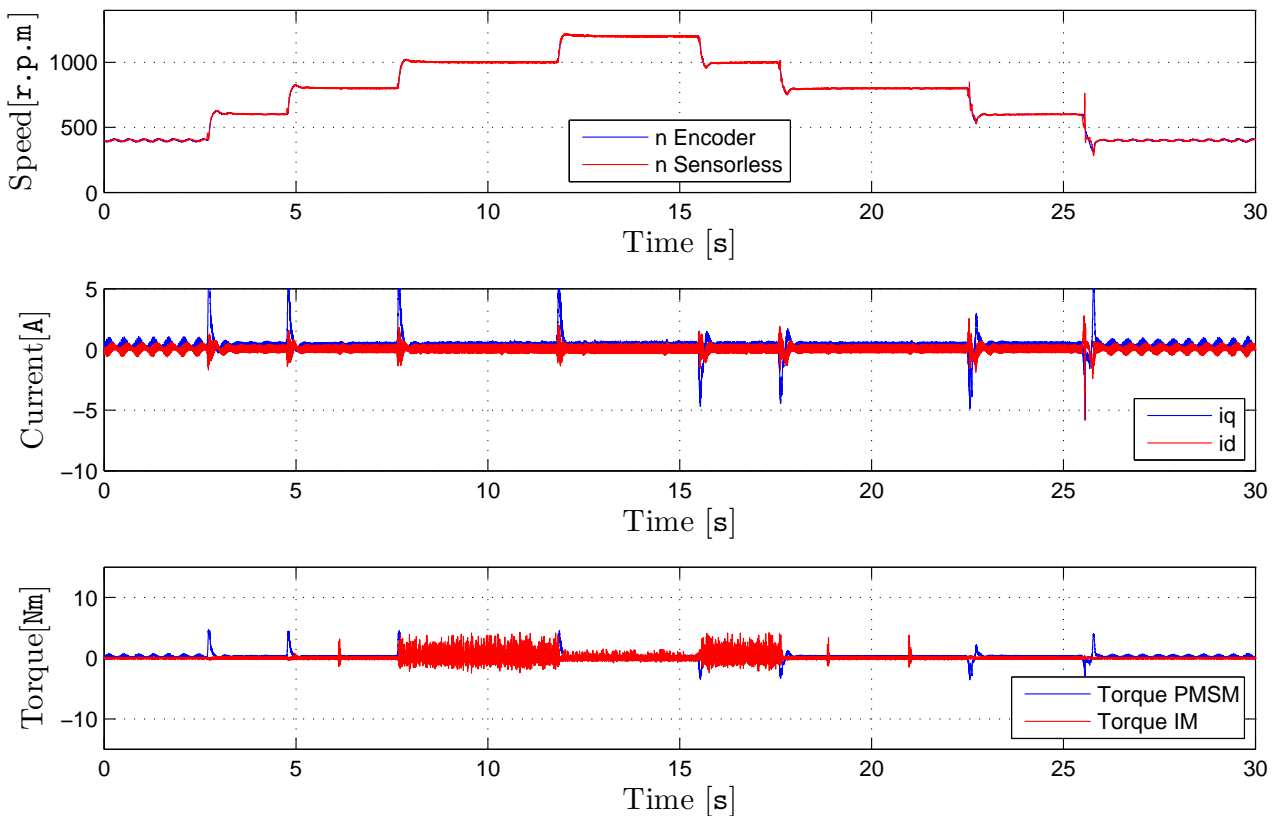
Figure 5.1. Experimental speed, torque, and current, in dq reference frames, responses.
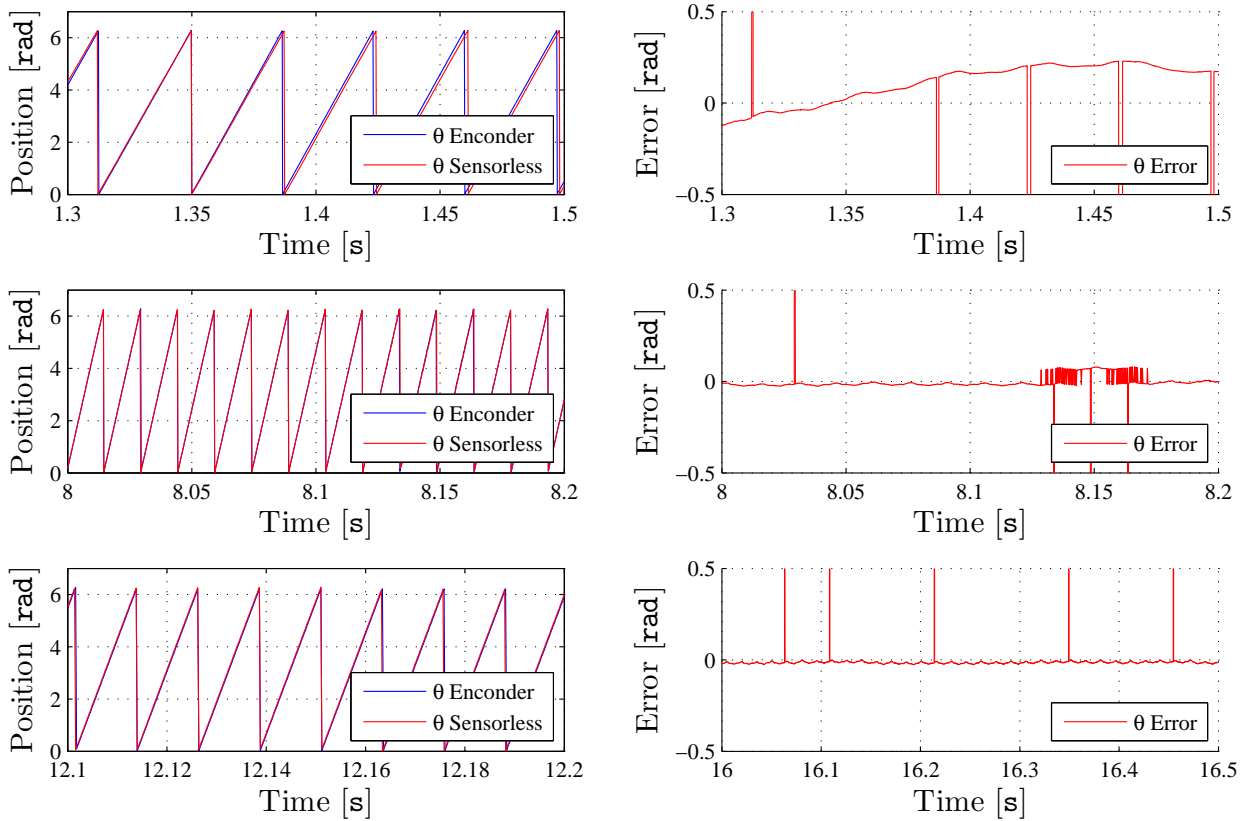
Figure 5.2. Experimental estimated angle response compared with the real angle response (right). Position error of the estimated angle response (left).

In the graph from the figure 5.1, it can be seen how the speed is increasing from 300 rpm until 1200 rpm by steps of 200 rpm. A good response in both steady and dynamic states is noticeable. The graph of the i_{dq} current takes the angle of the position estimation. The id current follows the zero reference, while, on the other hand i_q differs from zero in order to face the torque produced by T_{load}, B_m, J_0 and J_m. When there are changes in speed due to inertia, peaks in the i_q values appear. Finally, the graph of the Torque is shown in order to verify that there is no load, and to demonstrate how this affects the current.

Figure 5.2 shows the position estimation and the error for three different speeds. In these three cases, the error is almost negligible. In the first case there is an oscillation that can be produced due to the value of C_1 which is auto tuned to be very low.

5.1.2   Decreasing and increasing steps at negative speeds.

The motor is tested now at a negative speed to verify that it has the same response. Figures 5.3 and 5.4 show that the behavior is almost the same for both.

Therefore it is verified that the response is appropriate for the position and speed estimation, and correct operation of the auto tuning is seen when the sensorless control of the PMSM in running without any load.
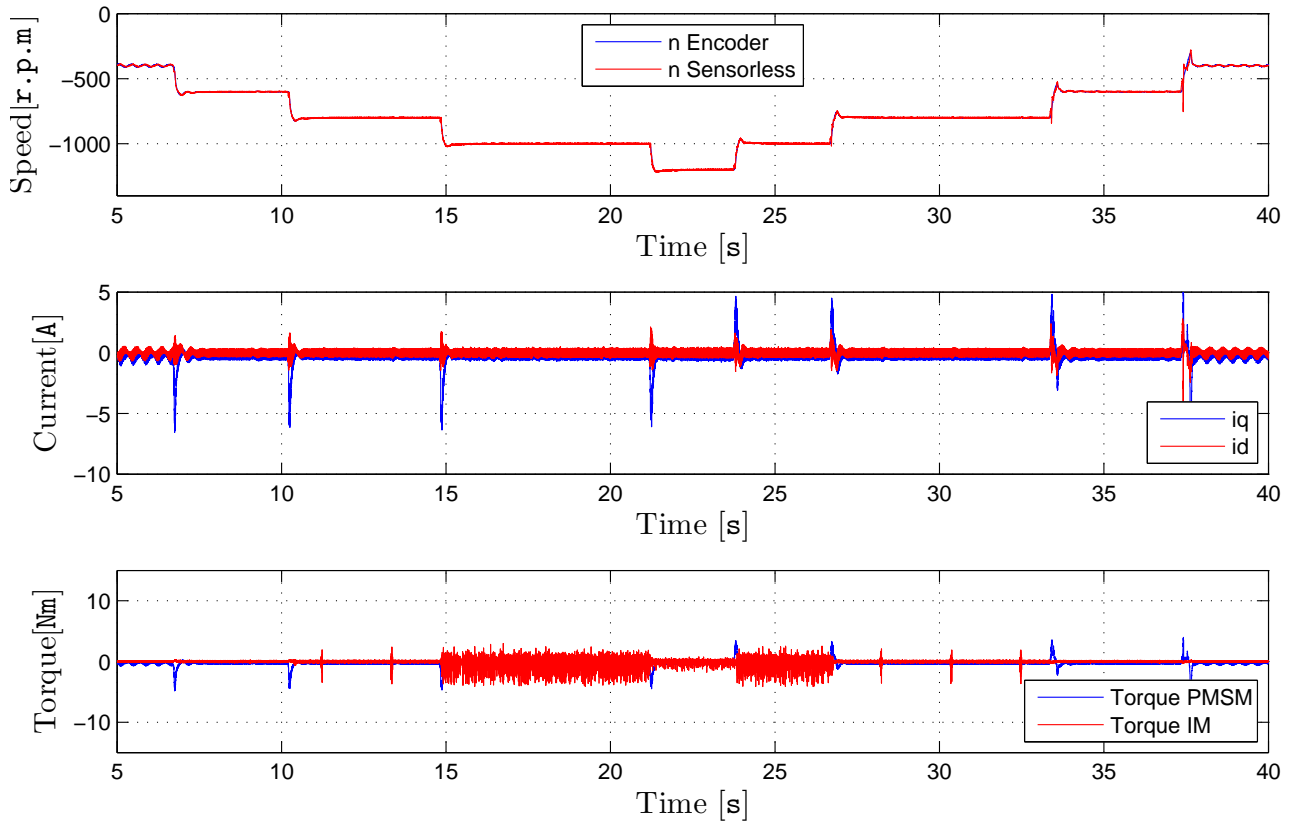
Figure 5.3. Experimental speed, torque, and current, in dq reference frames, responses.

Where figures 5.3 and 5.4 show that the behavior is almost the same for positive and negative values.
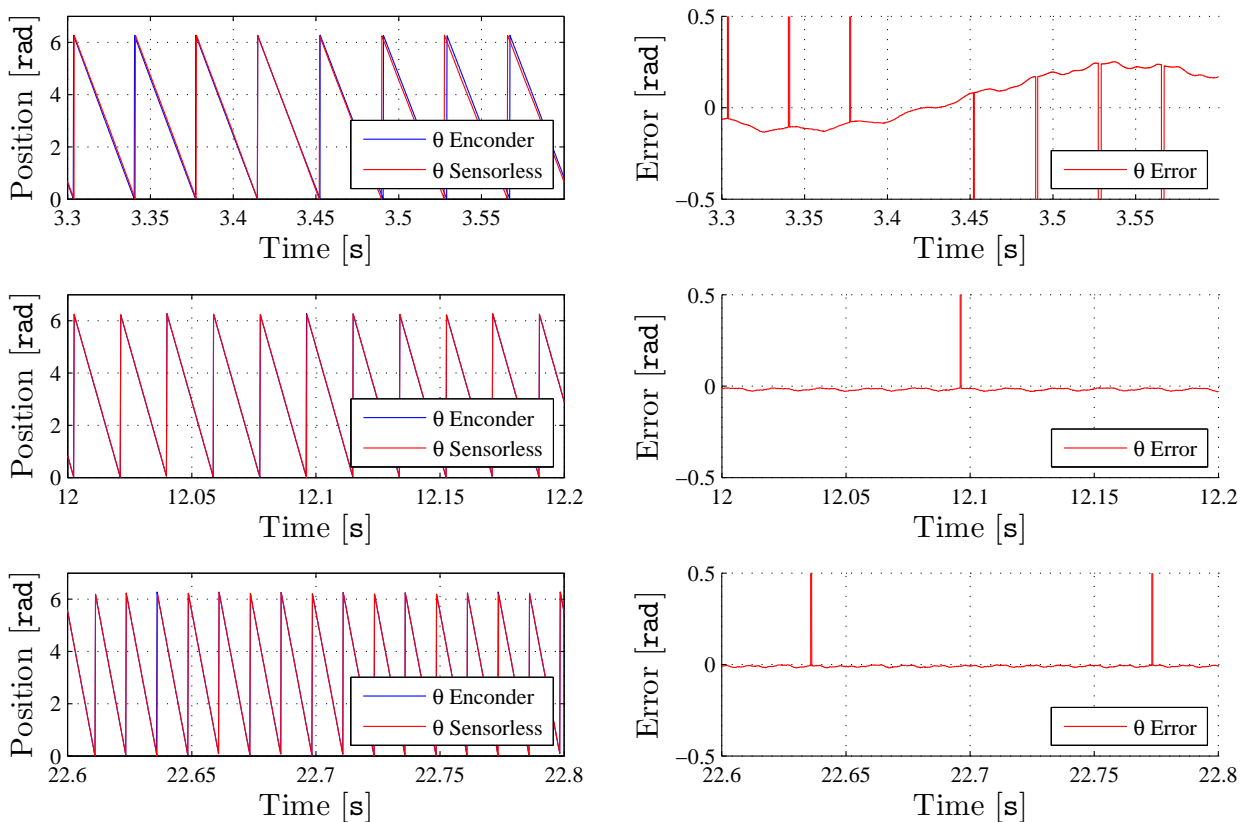

Figure 5.4. Experimental estimated angle response compared with the real angle response (right). Position error of the estimated angle response (left).

5.2 Speed steps with constant load torque.

In this case speed steps are applied with a constant 10 Nm torque as a load. After the torque is commanded speed steps are applied increasing and decreasing the values of it.
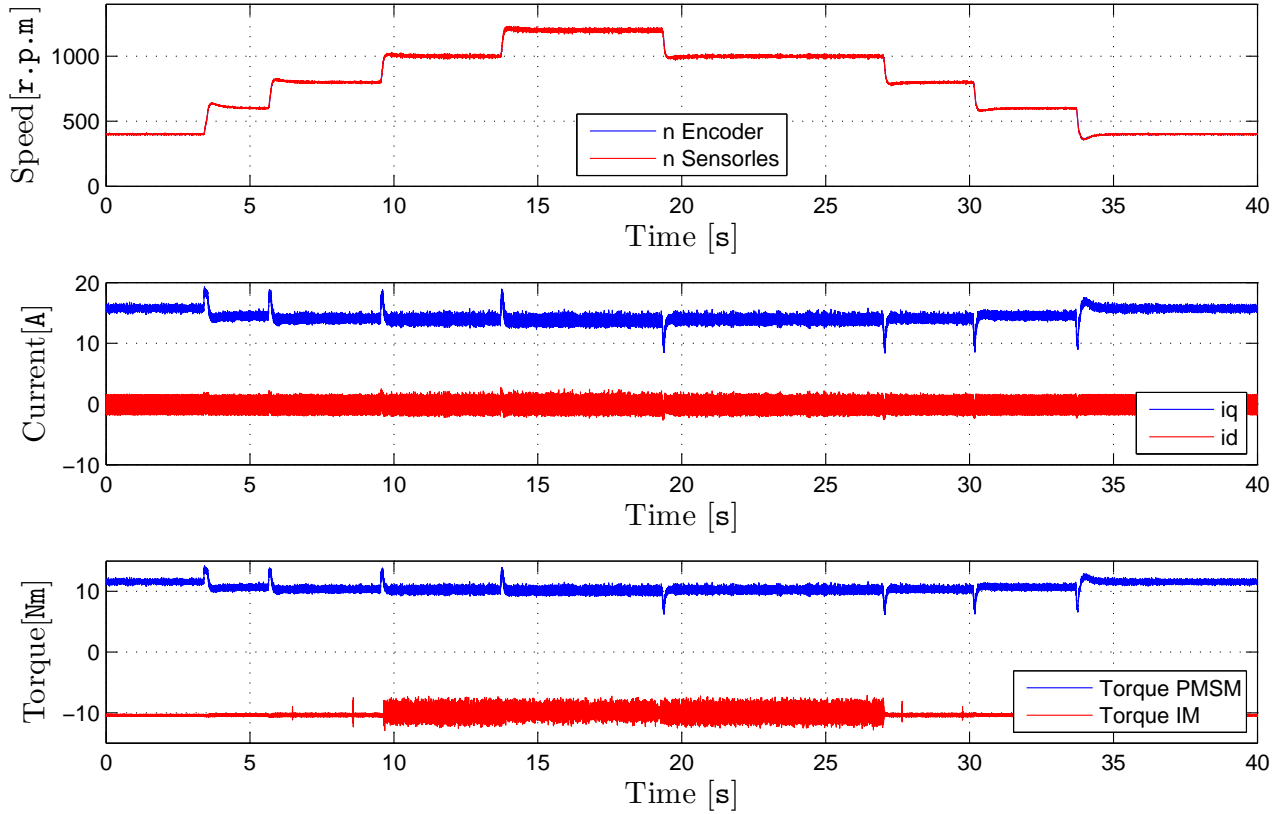
Figure 5.5. Experimental speed, torque, and current, in dq reference frames, responses.

Figure 5.5 shows how the speed responds properly for all speed ranges. In this case, in contrast to the preceding case, when a load is applied the behavior of the estimated speed response is better. This can be explained because of the higher current demand.

Figure 5.6 shows seen the currents abc stationary reference frames for different speeds, where the response is correct.

The position estimation shows an error that is corrected for increasing speeds. If there is a difference between λ_{pm} and λ_{dq} the error increases with lower speeds in accordance with the equations 4.15 and 4.13

This error is transformed by losses as it can be observed from figure 5.5 (current in dq reference frames graph). These losses are shown by the torque having a higher value than the one that is applied by the load.
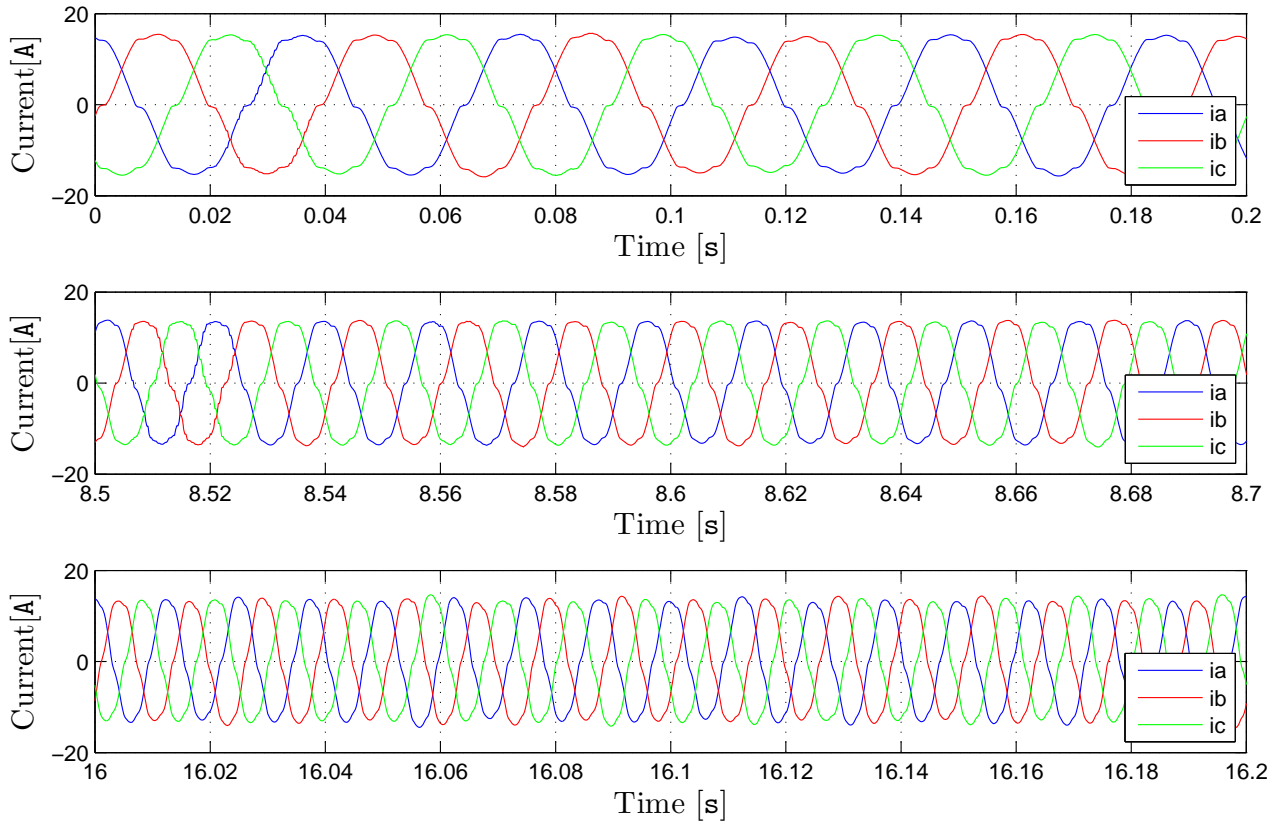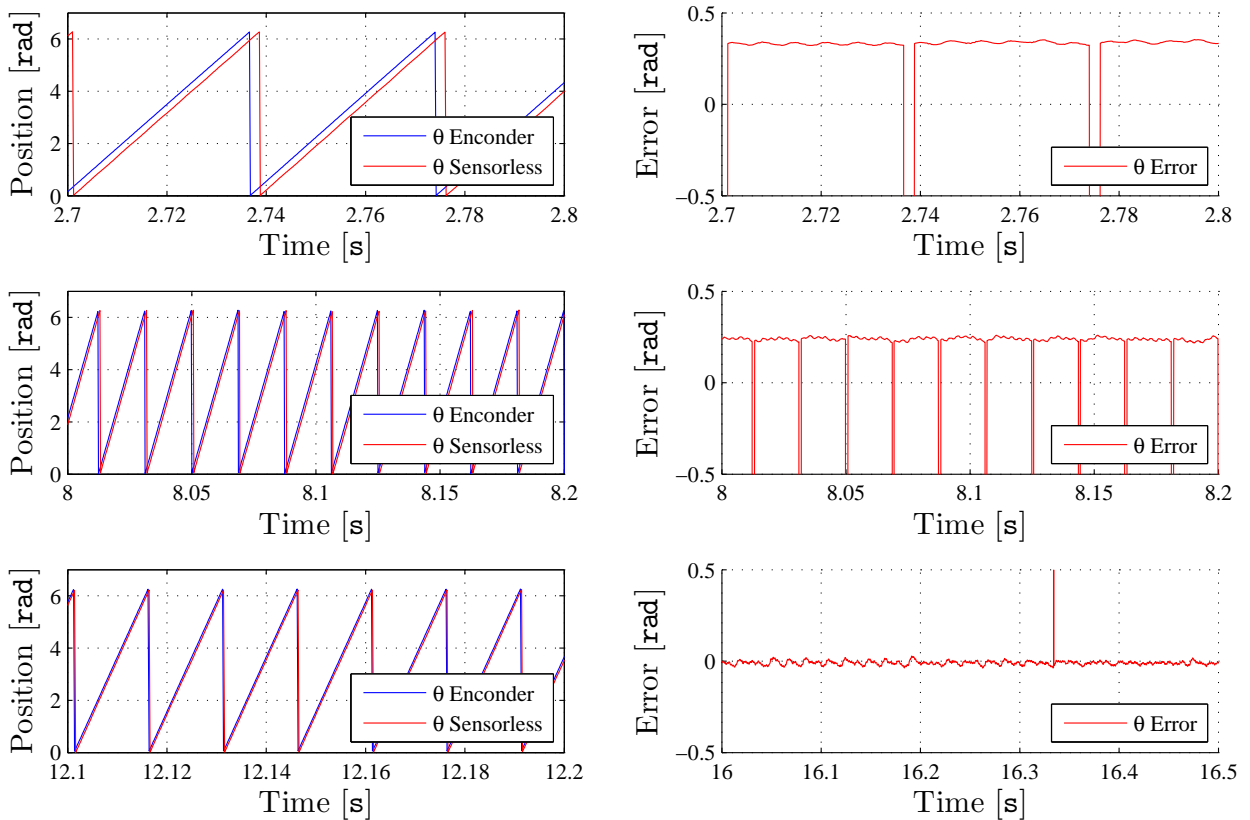
Figure 5.6. Experimental currents in abc stationary reference frames.

Figure 5.7. Experimental estimated angle response compared with the real angle response (right). Position error of the estimated angle response (left).

5.3   Constant speed command with load torque steps.

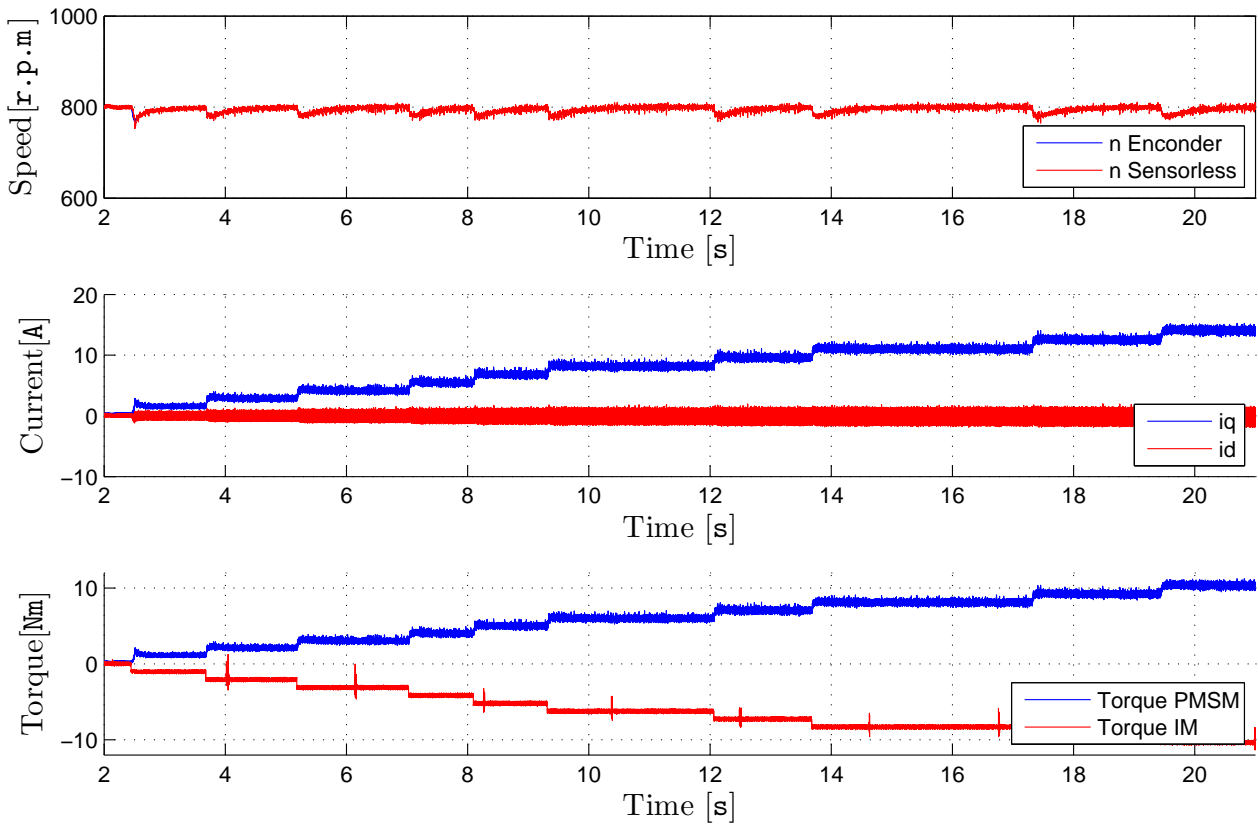In the final case the PMSM behavior with constant speed and applying torque steps is studied.

Figure 5.8. Experimental speed, torque, and current, in dq reference frames, responses.

Figure 5.8 shows the i_{dq} current and torque responses. The value of the speed corresponds to the frequency of the sinusoidal signal of the i_{abc} currents shown in figure 5.9. The i_{dq} current value shows the corresponding values of the current for different load values where the i_d current is kept constant and equal to 0 and the i_q current varies in function of the torque. That explains the correct position estimation. In figure 5.10, the estimated and the real angle positions are measured for different load values and for the variation interval of torque between 7 and 8 Nm in order to test the stationary and the dynamic state response.
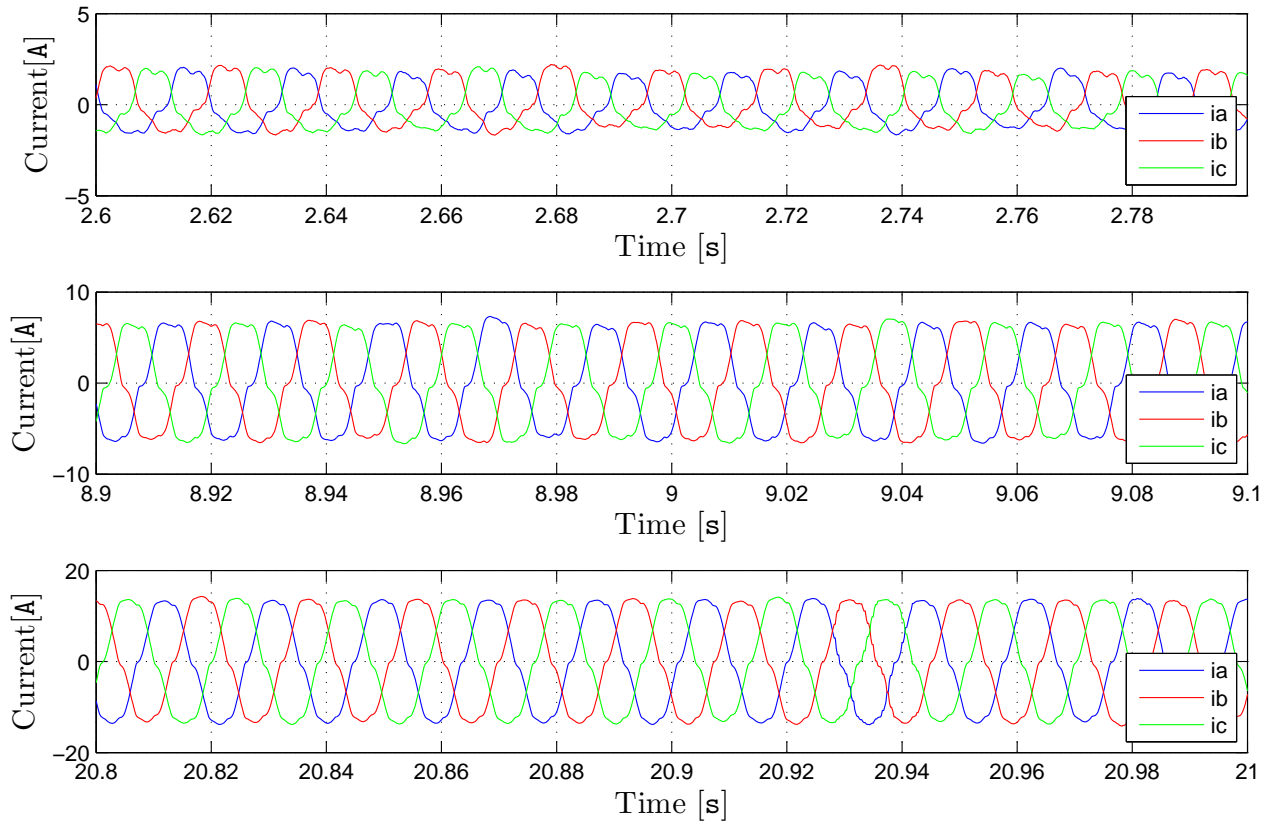
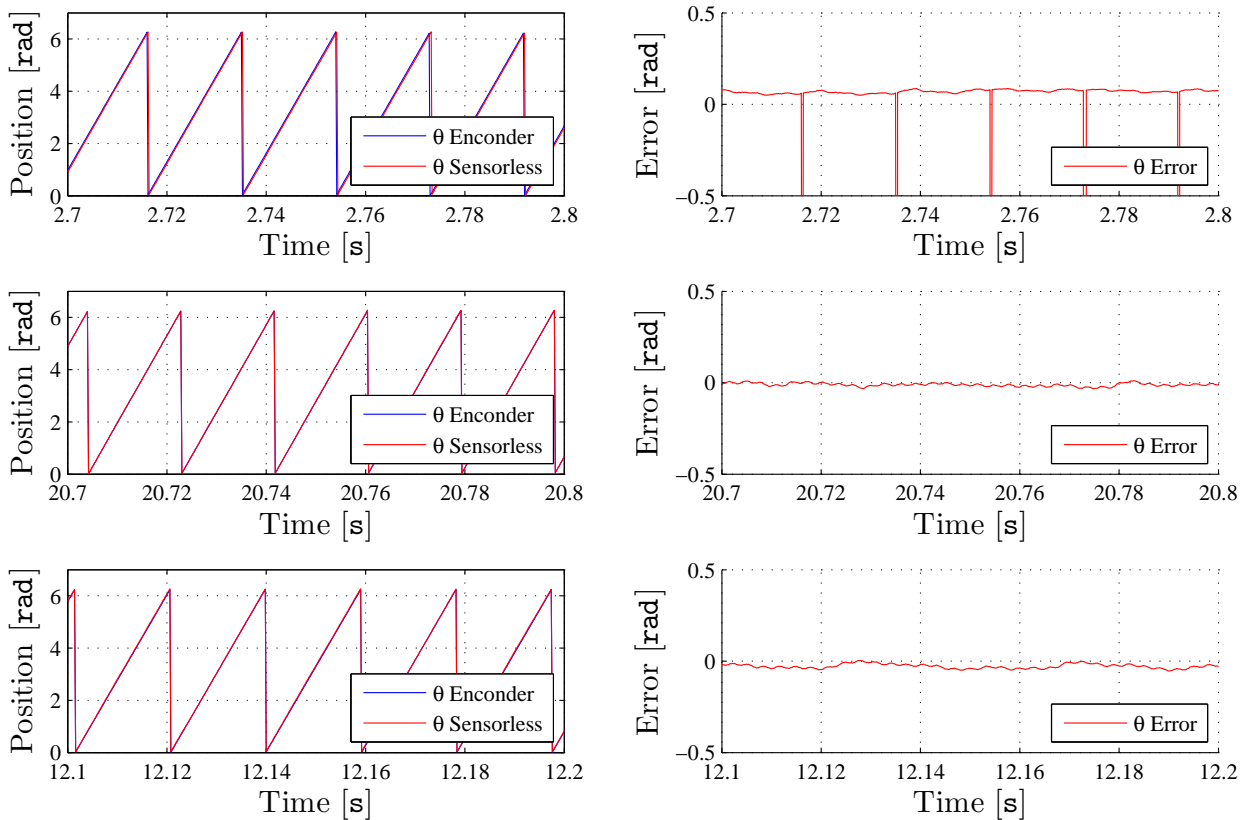**Figure 5.9.** Experimental steady state currents in abc stationary reference frames.

Figure 5.10. Experimental estimated angle response compared with the real angle response (right). Position error of the estimated angle response (left).

Chapter 6

Conclusion

FOC is the procedure used to control the machine while the park's transformations are used to simplify the control. The current PI controllers are tuned by applying Internal Model Control (IMC), and a speed PI controller is tuned, considering the requirements of the system. BEMF contribution is decoupled and the known dSPACE delays and drop voltage are considered in the simulations. An anti-windup is introduced in order to prevent possible damage to the machine.

Sensorless control is used in order to eliminate the sensor which has advantages in terms of reliability, machine size, noise and cost. Back-EMF is the method selected to be implemented to estimate the position using the stationary $\alpha\beta$-reference frames where the integral in equation 4.1 that is used to estimate the position, can cause a drift which occurs because of inaccurate measurements of the parameters or because of a small drift in the current. This can be eliminated using different methods. The methods Compensation block and Rasmussen are compared as they use different ways to solve the problem produced by the drift. An integral gain is added in the Rasmussen (Rasmussen PI) method in order to improve the response and eliminate the constant error, if present, but it causes a problem in terms of stability as is explained in Chapter 4.

The Back-EMF Rasmussen is the selected method to estimate the position because of the simplicity in the control and because it is the most recently developed method where the parameter C_1 need to be tuned in order to obtain an accurate response.

C_1 can be controlled according to the speed, "the higher C_1, the higher speeds that could be reached and vice versa for lower speeds".

Phase-locked loop (PLL) is the method selected to be implemented to estimate the speed where the PI_{PLL} controller needs to be tuned. The PI_{PLL} controller can be tuned according to the bandwidth.

Using 4.35 and 4.36, the theory demonstrates that the bandwidth is too large which causes a problem when higher frequencies than ω_r appear in the estimation of the rotor position. The undesired frequencies are eliminated by dividing the Bandwidth by $2 \cdot \pi$ and using the equations 4.45 and 4.39 to achieve a faster response, increasing K_{ep} and K_{ei} by a factor of ten. A new and more appropriate bandwidth for fulfilling the condition of 4.33 is achieved.

The delay that appears in the feedback of the system from the estimated position and the speed should be considered. The delay is considered at the worst case, that is when the machine is running at the lower speed (n = 200 rpm). The new speed PI controller's K_{wi} and K_{wp} are considered achieving the requirements of the system for FOC.

A position error $\overline{\theta}_{err}$ can be caused when the core of the machine is saturated, which occurs when the machine requires a high current. The theory is verified experimentally as is shown in Figures 4.9, 4.10 and 4.11 and the error is reduced successfully by 50% using equation 4.24 and 4.26.

The position error $\overline{\theta}_{ras}$ has to be considered since the Rasmussen method is used. Notice that the error can be kept constant if the ratio $C_1/\overline{\omega}$ is kept constant.

The Auto-tuning for the position estimation is done, tuning C_1 for the worst-case scenario study (n = 200 rpm) and setting constant, the ratio C_1 divided by $\widehat{\omega}$ considering $\widehat{\omega} = \omega^*$. Therefore C_1 can be tuned as a function of ω^*.

The Auto-tuning for the speed estimation is done considering the bandwidth as a function of ω^* using equations 4.35, 4.36, 4.45 and 4.39.

Therefore, the Auto-tuning is implemented for both position and speed estimation. It consists of the on-line control of the parameters C_1 for the position estimation method, and K_{ep} and K_{ip} for the speed estimation method, based on speed reference using the equation 4.46 for the auto-tuning of C_1 and 4.44 and 4.45 for the K_{ep} and K_{ip} respectively.

In Chapter 5, results for the sensorless rotor Feld Oriented Control of PMSM are presented for several setup scenarios, where the position and the speed are measured using the encoder in order to verify the results obtained by the Auto-tuning sensorless control.

The results are accurate for a range of speeds from -1400rpm to -300rpm and from 300 rpm to 1400, supporting a load of $\pm$ 10 Nm.

When no load is applied there is almost no error in the position and the speed estimation, but at low speed a big oscillation appears. On the other hand, when load is applied no oscillations appear but position error increases. Overall, the control operated correctly, achieving satisfactory results.

Chapter 7

CD Content

- Report(PDF)
- Simulink Model
- dSPACE Model
- System Data Tests
- References and literature

Bibliography

[1] Andres Lopez-Aranguren Oliver, Cesar Hernaez, E. B. N. J. M. (2013). Auto-tuning of high performance vector controller for pmsm drive system.

[2] Chen, J.-L. C. T.-H. L. C.-L. (2009). Design and implementation of a novel high-performance sensorless control system for interior permanent magnet synchronous motors.

[3] de Ciencias Basicas Universidad Iberoamericana, D. (2000). Control de modelo interno.

[4] Fabio Genduso, Rosario Miceli, M. I. C. R. and Galluzzo, G. R. (2000). Back emf sensorless-control algorithm for high-dynamic performance pmsm.

[5] H. Rasmussen, P. . V. a. and Brsting, H. (2012). Sensorless field oriented control of a pm motor including zero speed.

[6] Hernaez, C. (2014). Snsorless control of pmsm.

[7] Ion Boldea, Fellow, I. M. C. P. and Gheorghe-Daniel Andreescu, Senior Member, I. (2008). Active flux concept for motion-sensorless unified ac drives.

[8] Javier Fernndez Martnez, T. P. S. (2011). Low speed open loop field oriented control for permanent magnet machines.

[9] Jordi Espina, Toni Arias, J. B. C. (2006). Speed anti-windup pi strategies review for field oriented control of permanent magnet synchronous machines.

[10] Kaiyuan Lu, A. (2014). Modern electrical machine and drive systems sensorless control of pm machines.

[11] Kaiyuan Lu, Member, I. X. L. and Frede Blaabjerg, Fellow, I. (2008). Artificial inductance concept to compensate nonlinear inductance effects in the back emf-based sensorless control method for pmsm.

[12] O. Benjak, D. G. (2010). Review of position estimation methods for ipmsm drives without a position sensor.

[13] Pedersen, A. R. (2012). Comparison of back-emf based methods for sensorless control of a pmsm.

[14] Phillips, C. L. and Harbor, R. D. (2000). Feedback control systems. prentice hall.

[15] Phillips, C. L. and Harbor, R. D. (2011). Feedback control systems.

[16] P.S Frederiksen, J. Birk, F. (1994). Control and instrumentation for pm-machines.

[17] Remus Teodorescu, Marco Liserre, P. R. (2011). Grid converters for photovoltaic and wind power systems.

[18] Wang, D. (2013). Introduction of synchronous reluctance machine.

[19] Zihui Wang, Student Member, I. K. L. and Frede Blaabjerg, Fellow, I. (2012). A simple startup strategy based on current regulation for back-emf-based sensorless control of pmsm.

[20] Zihui Wang, Qinfen Lu, Y. Y. K. L. Y. F. (2000a). Investigation of pmsm back-emf using sensorless control with parameter variations and measurement errors.

[21] Zihui Wang, Kaiyuan Lu, Y. Y. Y. J. W. H. (2000b). Analysis of influence on back-emf based sensorless control of pmsm due to parameter variations and measurement errors.

Appendix A

VSI modulation strategy

The two level three phase Voltage Source Inverter is controlled by using SVM. SVM is used in the system due to the advantages such as it improves the DC-link utilization by 15.5% The Figure A.2 represent the phase voltage space vectors.
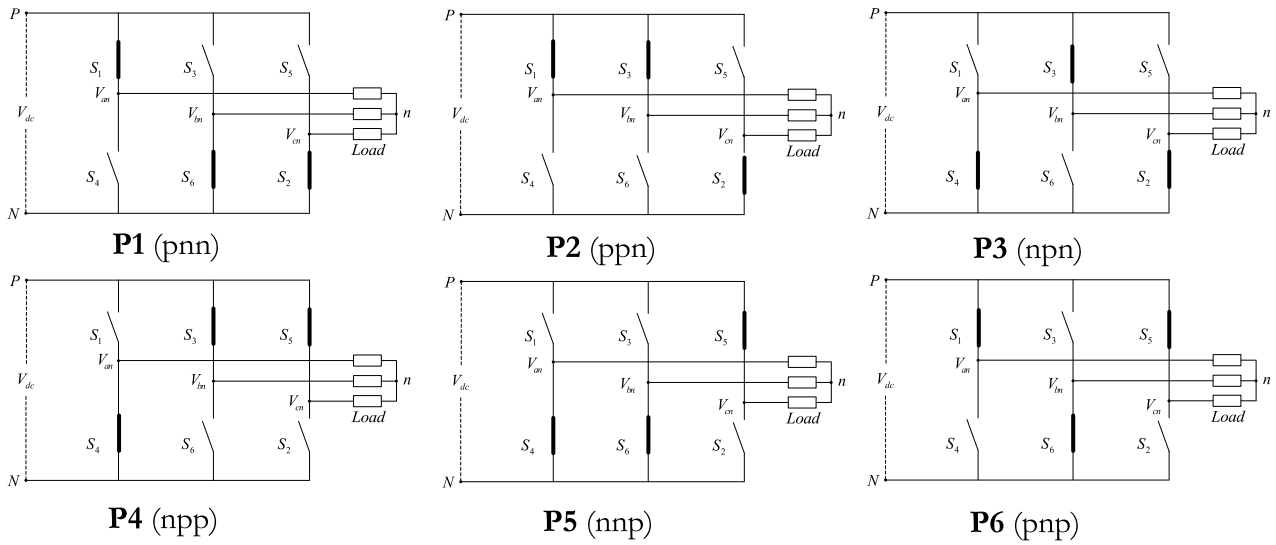

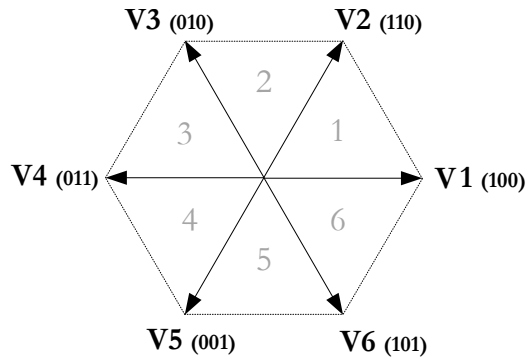**Figure A.1.** Space vector representation of inverter.

Figure A.2. Space vector representation of inverter.

Eight switch combinations can be applied according to the inverter switching position. Six distinct non-zero voltage switching positions (non-zero output voltages) and tho zero voltage switching position (zero output voltage).

The hexagon from the Figure A.2 show the six active vector, where the plane is divided into six sectors of 60 degrees each one. With maximum vlotage of $\frac{2}{3}V\_dc$

As an example Figure A.3 show the first vector that is formed by two non-zero output voltages, V1 and V2. The position vector can be determinate, in each space place, by controlling the duty cycles d_x d_y and d_0. Therefore the duty cycles should be calculated.
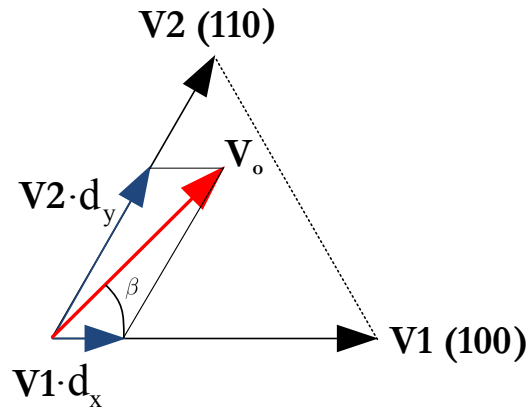

Figure A.3. Example of vector projection of the space vector.

Where d_x d_y are calculated by the follow equations:

$$V_o = d_x \cdot V1 + d_y \cdot V2 = d_x \cdot V1 + d_y \cdot V2 \cdot e^{j60} \qquad \text{[V]}$$

(A.1)

$$V_o = V_o \cos\beta + jV_o \sin\beta = d_x \cdot V1 + d_y \cdot \left(\frac{1}{2}V2 + j\frac{\sqrt{3}}{2}V1 \right) \qquad \text{[V]}$$

(A.2)

$$d_x = \frac{\sqrt{3} \cdot V_o \cdot 2}{V1 \cdot 3} \sin(60 - \beta) \qquad \text{[s]}$$

(A.3)

$$d_y = \frac{\sqrt{3} \cdot V_o \cdot 2}{V2 \cdot 3} \sin(\beta) \qquad \text{[s]}$$

(A.4)

Knowing d_x d_y the zero vectors d_o is calculated:

$$d_o = 1 - d_x - d_y \qquad \text{[s]}$$

(A.5)

Appendix B

Back-EMF method

The synchronous dq reference frame voltage equations for the PMSM are:

(B.1)
$$v_{qs}^r = R_s \cdot i_{qs}^r + \frac{d}{dt} \cdot \lambda_q + \omega_r \cdot \lambda_d$$
$$v_{ds}^r = R_s \cdot i_{ds}^r + \frac{d}{dt} \cdot \lambda_d - \omega_r \cdot \lambda_q$$
[V]

λ_d and λ_q are obtain cosidering the permanent magnets flux align with the d-axis in the dq-reference frame.

(B.2)
$$\lambda_d = L_d \cdot i_{ds}^r + \lambda_{pm}$$
$$\lambda_q = L_q \cdot i_{qs}^r$$
[V]

$\bar{v}_{dqs}^r$ and $\bar{\lambda}_{dq}$ are wrote as vectors in the equations B.3 and B.4.

(B.3)
$$\bar{v}_{dqs}^r = R_s \cdot i_{dqs}^r + \frac{d}{dt}(\lambda_{dq}) + j \cdot (\lambda_{dq}) \cdot \omega_r$$
[V]

(B.4)
$$\bar{\lambda}_{dq} = L_d \cdot i_{ds}^r + \lambda_{pm} + j \cdot L_d \cdot i_{qs}^r$$
[V]

The voltage in $\alpha\beta$ stationary reference frames show in the equation B.5 contain the flux linkage in $\alpha\beta$ stationary reference frames.

(B.5)
$$\bar{v}_{\alpha\beta s}^r = R_s \cdot \bar{i}_{\alpha\beta s}^r + \frac{d}{dt}(\bar{\lambda}_{\alpha\beta})$$
[V]

It can be obtain by using the equation B.4 and the electrical position of the rotor.

(B.6)
$$\bar{\lambda}_{\alpha\beta} = (L_d \cdot i_{ds}^r + \lambda_{pm} + j \cdot L_d \cdot i_{qs}^r)e^{j\theta}$$
[V]

Making the following transformation:

(B.7)
$$\bar{\lambda}_{\alpha\beta} = (L_d \cdot i_{ds}^r + \lambda_{pm} - L_q \cdot i_{ds}^r + L_q \cdot i_{ds}^r + j \cdot L_d \cdot i_{qs}^r)e^{j\theta}$$
[V]

(B.8)
$$\bar{\lambda}_{\alpha\beta} = (L_q \cdot \bar{i}_{\alpha\beta s}^r + [(L_d - L_q) \cdot i_{ds}^r + \lambda_{pm}]e^{j\theta}$$
[V]

And knowing that Ld and Lq are equal, the electrical position of the rotor can be obtain using $\alpha\beta$ components.

(B.9)
$$\angle\left[(L_d - L_q) \cdot i_{ds}^r + \lambda_{pm}\right] e^{j\theta} = \angle e^{j\theta} = \angle\bar{\lambda}_{\alpha\beta} - L_q \cdot \bar{i}_{\alpha\beta s}^r \qquad [\text{V}]$$

(B.10)
$$\theta = \tan^{-1}\left(\frac{\lambda_\beta - L_q \cdot i_{\beta s}^r}{\lambda_\alpha - L_q \cdot i_{\alpha s}^r}\right) \qquad [\text{V}]$$

(B.11)
$$\lambda_\beta = \int (v_{\beta s}^r - R_s \cdot i_{\beta s}^r) dt$$
$$\lambda_\alpha = \int (v_{\alpha s}^r - R_s \cdot i_{\alpha s}^r) dt \qquad [\text{V}]$$

(B.12)
$$\theta = \tan^{-1}\left(\frac{\int (v_{\beta s}^r - R_s \cdot i_{\beta s}^r) dt - (L_q \cdot i_{\beta s}^r)}{\int (v_{\alpha s}^r - R_s \cdot i_{\alpha s}^r) dt - (L_q \cdot i_{\alpha s}^r)}\right) \qquad [\text{V}]$$